POST-PRINT

A multi-dating approach to age-modelling long continental records: the 135 ka El Cañizar de Villarquemado sequence (NE Spain)

2

3

4 B.L. Valero-Garcés1,2; P. González-Sampériz1; G. Gil Romera1,3; B. M. Benito4; A.

5 Moreno1,2; B. Oliva-Urcia5; J. Aranbarri6; E. García-Prieto1; M. Frugone7,2; M. Morellón8;

6 L.J. Arnold9; M. Demuro9; M. Hardiman10; S.P.E. Blockley11; C.S. Lane12

7 1. Pyrenean Institute of Ecology (IPE) – CSIC. Avda Montañana 1005. E-50059 Zaragoza, Spain.

8 2. Laboratorio Internacional de Cambio Global, CSIC, PUC, UFRJ, Avda Montañana 1005. E-50059

9 Zaragoza, Spain.

10 3. Department of Geography and Environmental Sciences, Llandinam building, Penglais Campus.

11 Aberystwyth University SY233DB, Aberystwyth, United Kingdom.

12 4. Ecological and Environmental Change Research Group, Department of Biological Sciences,

13 University of Bergen, Norway.

14 5. Department of Geology and Geochemistry, Faculty of Sciences, Universidad Autónoma de

15 Madrid. C/ Francisco Tomás y Valiente 7. Campus de Cantoblanco, E-28049 Madrid, Spain.

16 6. Department of Geography, Prehistory and Archaeology, University of the Basque Country,

17 Francisco Tomás y Valiente, s/n. E-01006 Vitoria-Gasteiz, Spain.

18 7. Department of Ecology. Pontificia Universidad Católica de Chile, Avda. Alameda, Santiago,

19 Chile.

20 8. CITIMAC, University of Cantabria. Avenida de los Castros s/n. E-39005 Santander (Cantabria),

21 Spain.

22 9. School of Physical Sciences, Environment Institute, and Institute for Photonics and Advanced

23 Sensing (IPAS), University of Adelaide, North Terrace Campus, Adelaide, SA, 5005, Australia.

24 10. Department of Geography, University of Portsmouth, Portsmouth, PO1 3HE, UK.

25 11. Centre for Quaternary Research, Department of Geography, Royal Holloway, University of

26 London, Egham, Surrey, TW2 0SE, UK.

27 12. Department of Geography, University of Cambridge, Downing Place, Cambridge, CB2 3EN, UK.

28

29 ABSTRACT.

30 We present a multidisciplinary dating approach - including radiocarbon,

31 Uranium/Thorium series (U/Th), paleomagnetism, single-grain optically stimulated

32 luminescense (OSL), polymineral fine-grain infrared stimulated luminescence (IRSL) and tephrochronology -

33 used for the development of an age model for the Cañizar de Villarquemado sequence

34 (VIL) for the last ca. 135 ka. We describe the protocols used for each technique and

35 discuss the positive and negative results, as well as their implications for interpreting

36 the VIL sequence and for dating similar terrestrial records. In spite of the negative

37 results of some techniques, particularly due to the absence of adequate sample

38 material or insufficent analytical precision, the multi-technique strategy employed

39 here is essential to maximize the chances of obtaining robust age models in terrestrial

40 sequences. The final Bayesian age model for VIL sequence includes 16 AMS 14C ages, 9

41 single-grain quartz OSL ages and 5 previously published polymineral fine-grain IRSL ages, and the accuracy and resolution of the

42 model are improved by incorporating information related to changes in accumulation

43 rate, as revealed by detailed sedimentological analyses. The main paleohydrological

44 and vegetation changes in the sequence are coherent with global Marine Isotope Stage

45 (MIS) 6 to 1 transitions since the penultimate Termination, although some regional

46 idiosyncrasies are evident, such as higher moisture variability than expected, an abrupt

47 inception of the last glacial cycle and a resilient response of vegetation in

48 Mediterranean continental Iberia in both Terminations.

49

50 KEYWORDS: Bayesian Age model, Radiocarbon, OSL, IRSL, Last Glacial Cycle,

51 Mediterranean, Continental sequences

52

53

1. INTRODUCTION

Major advances in paleoclimate research have been made possible only after improving numerical dating methods, reducing the time uncertainties of reconstructed changes and consequently facilitating our ability to precisely compare ice, marine and terrestrial records along spatial and temporal transects. Only with independent and robust age models we can test 'leads' and 'lags' in teleconnections between the atmospheric, marine, terrestrial and cryospheric realms (Hoek et al., 2008) and understand spatial patterns and mechanisms behind abrupt climate fluctuations, such as those documented within the last glacial cycles (Broecker, 2000).

During the last decades, the scientific community has made a significant effort to recover new, long continental sequences, extending beyond the last glacial cycle from classical sites such as Grande Pile (Woillard, 1978), Les Echets (de Beaulieu and Reille, 1989), Velay (Reille et al., 2000), Monticchio (Allen and Huntley, 2009), Ioannina (Tzedakis et al., 2003), or Tenaghi Philippon (Tzedakis et al., 2006). Several outstanding long sequences have been obtained thanks to international initiatives such as the International Continental Scientific Drilling Program (ICDP, https://www.icdp-online.org/home/) (e.g., Lake Titicaca (Fritz et al., 2007), Potrok Aike (Zolitschka et al., 2013), Dead Sea (Stein et al., 2011), Lake Van (Litt et al., 2009), Petén Itzá (Hodell et al., 2008), El'gygytgyn (Melles et al., 2012), Lake Ohrid (Lézine et al., 2010; Zanchetta et al., 2016), Lake Chalco (Brown et al., 2012), Lake Junin (Rodbell and Abbott, 2012), and Towuti in Indonesia (Rusell et al. 2016). These long sequences span several glacial cycles and contain a detailed history of changes in vegetation, environmental and climate. However, in all cases, obtaining a robust chronology has remained a challenge. The exceptions to this rule are the long, continuous, annually laminated

78 terrestrial records able to produce absolute and independent varve chronologies, such

79 as Lake Suigetsu in central Japan for the last 70,000 years (Ojala et al. 2012) or well-

80 dated speleothems that accurately cover long time periods, sometimes with excellent

81 resolution (Wang et al., 2001; Pérez-Mejías et al., 2017). Unfortunately, these records

82 are not common.

83 Due to the difficulties of obtaining independent, numerical, reliable and robust

84 chronologies, most of the well-known long traditional sequences rely on either directly

85 or indirectly tuning to orbital configurations or ice core chronologies (Tzedakis et al.,

86 2006, Blaauw, 2012). This tuning approach precludes the correct identification of either regional and

87 local particularities or potential leads and lags on different spatial and chronological

88 scales (Brauer et al., 2007).

89 A combination of different dating techniques depending on the age and type of

90 material is commonly applied to resolve the timing of past events in long terrestrial

91 sequences. Radiocarbon dating is the most commonly used for the last 50,000 years (50 ka).

92 although longer calibration curves have become available during the last decade

93 (Reimer et al., 2004, 2009, 2013)

94 Uncertainities of more than several hundred years are frequent, particularly beyond the

95 Last Glacial Maximum (LGM). Another common limitation of radiocarbon dating in terrestrial

96 sequences is the infrequent preservation of terrestrial organic remains suitable for

97 dating, particularly in semi-arid areas, as well as the occurrence of reworking processes

98 (González-Sampériz et al., 2008; Valero-Garcés and Moreno, 2011; Lionello et al.,

99 2012). U/Th series dating, commonly applied to speleothems, provides higher precision and longer time scales and it has been also used in

100 lacustrine sequences (Placzek et al., 2006a) but its applicability depends on the

101 presence of highly pure endogenic carbonate in the lacustrine sediments (Bischoff and

102 Cummins, 2001; Placzek et al., 2006a,b). Paleomagnetic dating based on geomagnetic

103 excursions, inclination and/or declination changes requires a minimum amount of

104 ferromagnetic minerals carrying a primary (i.e. acquired at the time of sedimentation)

105 magnetic signal that clearly defines the paleomagnetic characteristic components along

106 the sequence (Roberts, 2008). For measurements of declination, methods are

107 needed to precisely record the original orientation of sampled sediments, and the geographic location is also important for some magnetic properties. Tephras can

108 provide punctuated, numerical, highly accurate ages (e.g., Zanchetta et al., 2011), but

109 discrete ash-layers are not always preserved in terrestrial settings and even

110 cryptotephras are sometimes difficult to detect in lacustrine sediments (Davies, 2015).

111 Despite improvements in the identification and analysis of microscopic volcanic ash

112 layers and cryptotephras transported across very long distances (Blockley et al.,

113 2005; Lane et al., 2017), the use of this technique is spatially limited to regions where

114 material derived eruptions was deposited and

115 preserved. Tephra layers may serve as precise markers even when the age is unknown and the use of this technique can be extended to fingerprinting tephra of unknown source but distinctive geochemistry to correlate across regions. Luminescence dating techniques such as optically stimulated luminescence

116 (OSL) of quartz and infrared stimulated luminescence (IRSL) of feldspars only require a relatively small

117 amount of siliciclastic material to determine the burial age of terrestrial sediment

118 sequences (the last time since sunlight exposure). However, in spite of recent

119 developments, (e.g., single grain techniques or extended-range approaches; Murray

120 and Roberts, 1997; Arnold et al., 2015), the suitability of luminescence dating

121 techniques may be compromised by certain depositional or post-depositional

122 complications (e.g., incomplete resetting of residual signals prior to burial or post-depositional mixing; Arnold et al., 2008; Arnold and Roberts, 2009) and the analytical precision of these techniques (typically >5% at 1σ; e.g., Arnold and Demuro, 2018) is sometimes sub-

123 optimal for high-resolution studies (e.g. Fu et al., 2017; De Deckker et al., 2019).

124 In summary, most of the available dating methods in terrestrial sequences

125 require certain amounts of specific sediment components and it is unlikely that a single

technique can provide a universally robust, high resolution chronology. These various techniques do not necessarily date the same events and so it is critical to discuss how the dates relates to the relevant sedimentological and stratigraphic relationships when comparing the ages generated by different techniques. Additionally, a unique problem of long terrestrial records such as lacustrine sequences compared to marine or speleothem records is the larger temporal and spatial variability of sedimentary facies and depositional environments (Cohen, 2003). Within the same sedimentary basin and in the same site, even when located at the deepest part of the basin, depositional dynamics could have greatly changed during the last glacial cycles and sedimentation rates sometimes vary by several orders of magnitude. Thus, linear extrapolation of sedimentation rates without considering these changes in sedimentary facies produces age models with large errors.

In this paper we summarize the efforts to directly date and construct an robust age model for a long lacustrine sequence from Southwestern Europe: El Cañizar de Villarquemado paleolake (hereafter referred as VIL). The Iberian Peninsula constitutes a sensitive area to reconstruct past hydrological changes (Giorgi and Lionello, 2008; García-Ruiz et al., 2011; Valero-Garcés and Moreno, 2011 and references therein; Morellón et al., 2018) and due to its particular location, with the influence of mid latitude and sub-tropical forcings and a strong Mediterranean - Atlantic climatic gradient, it is a unique place to study the interplay of atmospheric patterns during the last glacial cycles (Lionello et al., 2012; Tzedakis, 2007) and their environmental impacts on the continents through the Late Quaternary (e.g., Carrión and Leroy 2010 and references therein; Magri et al., 2017). Previous research has demonstrated the potential of this site as a recorder of hydrological and vegetation changes in semi-arid continental regions of the Iberian Peninsula during the last ca. 120-130 ka (Moreno et al., 2012; González-Sampériz et al, 2013; Aranbarri et al., 2014; García-Prieto, 2015). VIL sequence (Figure1) extends back to Termination II and thus, constitutes a

reference site for Southern Europe paleoclimate and paleoenvironmental variations covering the last two glacial cycles. Here we present and discuss the multidisciplinary dating approach (including radiocarbon, U/Th, paleomagnetism, single-grain quartz OSL, polymineral fine-grain IRSL and tephrochronology) used for the development of the best possible age model for the VIL sequence over the last ca. 135 ka and discuss the main benchmarks used to produce such a model that might be useful for other similar long sequences. We explore the coherence of this age model against the available sedimentological data, preliminary selected pollen results, and other records from mid-latitudes.

2. REGIONAL SETTING

2.1. The Jiloca Basin

The 'El Cañizar de Villarquemado' wetland is located in the Iberian Range, Northeastern Spain (Figure 1A), at ca. 1000 m a.s.l., in the southernmost area of the 60 km long Jiloca Depression, an Upper Pliocene N-S half-graben bounded by NW-SE trending normal faults (Rubio and Simón, 2007). During the Quaternary, the northern areas of the Jiloca Basin changed to exorheic drainage progressively while in the southern area endorheic conditions remained (Gutiérrez-Elorza and Gracia, 1997) and a shallow (up to 2.8 m deep) lake developed, covering a maximum surface area of 11.3 km2 (Figure 1B) and becoming the largest freshwater lake in the Iberian Range and one of the largest in the Iberian Peninsula (Rubio, 2004). The lake was drained to the north during the 18th century to increase agricultural land and reduce flooded areas perceived as a source of mosquito-borne diseases (Rubio, 2004). The evolution of the lake basin has been controlled by tectonics, subsidence, and the depositional dynamics of two ephemeral streams to the north, the Villarrosano and Rebollos. As the basin sits

174 on Mesozoic limestones, variable karstic activity during the last millennia could also
175 have affected base level and influenced depositional history (Gracia et al., 2003;
176 Gutiérrez et al., 2008, 2012).
177 Current regional vegetation plant communities are mainly composed by oaks
178 (Quercus ilex rotundifolia, Q. faginea), junipers (Juniperus thurifera, J. phoenicea), and
179 pines (Pinus nigra, P. pinaster and P. sylvestris) as the dominant trees, depending on
180 altitude, exposure and soil type. Open Mediterranean xerophytic shrub communities
181 with Rhamnus alaternus, Genista scorpius, Ephedra fragilis, Thymus spp., Rosmarinus
182 officinalis and Artemisia assoana amongst others are also frequent. The wetland
183 surroundings are mostly cultivars. The climate of the region is Continental
184 Mediterranean with long cold winters, hot summers, and a large water deficit (López-
185 Martín et al., 2007).
186
187 2.2. The Cañizar de Villarquemado sediment (VIL) sequence
188 After an exploratory Livingstone extraction of ca. 2 m core length (VIL05-1A-1L),
189 a 74 m long core was recovered in 2005 with a truck–mounted drill rig in the central
190 area of the wetland (VIL05-1B-1T), where the basin depocenter was located (987 m
191 a.s.l, 40°30'N; 1°18'W). The sediment cores were split lengthwise in two halves and
192 imaged with a GEOTEK camera. High-resolution magnetic susceptibility profiles were
193 acquired with a GEOTEK multisensory core data logger at the Limnological Research Center, University
194 of Minnesota. Total Organic Carbon (TOC), Total Inorganic Carbon (TIC) and Total
195 Nitrogen (TN) measurement were performed in samples taken at 2 cm intervals. XRF
196 scanner measurements were performed every 4 cm with the ITRAX XRF at the Large

197 Lakes Observatory, University of Minnesota. Cores were correlated based on key

198 markers, facies and geochemical profiles.

199 Twenty facies were identified and described based on sediment composition,

200 textures, color and microscopic observations of smear slides following

201 Schnurrenberger et al. (2003). They correspond to four textural types (sand, coarse silt,

202 fine silt, organic-rich) (Table 1 and Figure 2) and have been grouped in four facies

203 associations (FA) and their interpreted depositional environments (FA): carbonate lake (A), clastic

204 lake (B), wetland (C) and alluvial (D) (described previously in Moreno et al., 2012;

205 González-Sampériz et al., 2013). The VIL sequence exemplifies the characteristic large

206 spatial and temporal variability of facies in shallow lacustrine basins (Cohen, 2003;

207 Valero-Garcés et al., 2011, 2014). In this setting, a variety of sub-environments occur

208 from distal alluvial fans (FA D), shallow carbonate ponds with charophyte meadows (FA

209 A), areas with dominant organic deposition (FA C), and other with higher clastic input

210 from the ephemeral or permanent inlets (FA B). Small changes in the hydrology, base

211 level or accommodation space in the basin cause a lateral migration of the sub-

212 environments. Development of a carbonate lake represents higher lake levels than

213 during wetland/peatland stages while alluvial fans prograded over the lake basin

214 during the lowest lake levels phases. Although bathymetric inferences from sediment

215 composition are not straightforward in these settings, clastic lake facies are

216 interpreted as reflecting relatively deep deposition compared to carbonate lake facies as they

217 require higher sediment and water input from the catchment area along small streams

218 and creeks (Valero-Garcés et al., 2014). Examples of modern shallow lake-wetland systems

219 are the Everglades in Florida (USA) or the Ruidera Lakes in Spain. Similar depositional settings have been described during the

220 Quaternary, particularly in the early development stages of large basins such as the Great
221 Salt Lake (Balch et al., 2005) and Titicaca (Fritz et al., 2007).
222 Seven sedimentary units have been defined in the sequence based on the
223 occurrence of facies association (Figure 2): Unit VII (74–56m depth) groups facies from
224 a depositional environment characterized as a mosaic of wetlands, peatlands and
225 carbonate lakes with high carbonate production; Unit VI (56–38m depth), contains
226 facies association B (clastic lakes) and C (wetlands); Unit V (38-29m depth) is
227 characterized by the retreat of the wetlands and the pro-gradation of the alluvial fans
228 over the distal areas of the lake basin (FA D and B); Unit IV (29-21m depth) is
229 dominated by distal alluvial fan and mud flat environments (FA D); Unit III (21–15m
230 depth) encompasses clastic lake (FA D) and distal alluvial fan facies (FA C); Unit II (15–
231 3m depth) contains both, clastic and carbonate lake facies associations (A and B); and
232 finally, Unit I (3-0m depth) represents a carbonate lake (FA A) with minor development
233 of wetland/peatland environments (FA C).
234
235 3. METHODS: A MULTI-DATING TECHNIQUE STRATEGY FOR AN AGE MODEL
236 We have applied a number of dating techniques to the VIL sequence, in order to obtain the
237 best possible independent age model: radiocarbon, U/Th series, single-grain quartz OSL, polymineral fine-grain IRSL,
238 paleomagnetism, and (crypto-) tephrochronology (Figure 2). In the next section we
239 describe for every methodology the sampling procedures (sample numbers, selection
240 criteria, etc.,) and the dating technique (chemical procedures, equipment, etc.).
241 3.1. Radiocarbon (AMS 14C)
242 A total of twenty three AMS radiocarbon ages were obtained for the VIL sequence (Table
243 2), twenty of them in the long core VIL05-1B-1T and three from the shorter parallel

244 core VIL05-1A-1L (Aranbarri et al., 2014). Sediment samples were collected as 1 cm-

245 thick sediment slices after detailed macroscopic descriptions and microscopic

246 observation of smear slides to check for terrestrial remains. However, due to the

247 absence of organic terrestrial macro-remains, all the analysed samples correspond to

248 bulk sediment from intervals with relatively high TOC content. Samples were analysed at the Poznan

249 Radiocarbon (Poland) and Beta Analytic (USA) laboratories following their respective protocols for pre-treatment and ages converted into

250 calendar years using the INTCAL13 calibration curve (Reimer et al., 2013).

251 3.2. U/Th series dating

252 Eleven samples were selected to run U/Th analyses (Table 3A). Firstly, we looked for

253 pure endogenic inorganic carbonates, but the only occurrence were small carbonate

254 coatings of aquatic plants and Chara fragments. We also selected well-preserved

255 gastropods, although U uptake or loss in biological material poses challenges to dating

256 (Bischoff and Cummins, 2001; Placzek et al., 2006a). Unfortunately, the number of

257 gastropods or biological carbonate coating pieces at discrete levels was never enough

258 to reach the minimum weight (ca. 100 mg) necessary for reliable U/Th analysis by ICP-

259 MS in samples with relatively low U content, and consequently samples from several

260 depths were combined (Table 3). Both biogenic coating carbonate particles and

261 gastropods were cleaned by physically removing any adhered detritus. Samples were

262 then treated with 6% NaOCl for 18–24 hr at room temperature to remove all organic

263 material and then washed repeatedly in “ultrapure” water, sonicated for a few

264 minutes to remove adhered solution, washed again, and dried in a vacuum oven

265 overnight at ~70 ºC. The chemical procedure used to separate the uranium and

266 thorium was carried out at the University of Minnesota (USA) laboratories following

267 standard methodologies (Edwards et al., 1987; Cheng et al., 2013). Analyses were

268 conducted by inductively coupled plasma mass spectrometry (ICP-MS) on a Finnigan-
269 MAT Element equipped with a double focusing sector-field magnet in reversed Nier–
270 Johnson geometry and a single MasCom multiplier from the University of Minnesota
271 laboratories.
272 3.3. Tephrochronology
273 To our knowledge, the VIL sequence was one of the first records from NE Spain tested for
274 cryptotephras. Based on a preliminary chronology (Moreno et al., 2012), the 4–24 m
275 depth interval corresponding to ca. 50-159 ka was sampled contiguously and analysed
276 for cryptotephra content. Facies sampled included clay and silt beds with some
277 interspersed fine sandy layers. Numerous techniques have been employed to detect
278 cryptotephra within sedimentary records. These techniques utilise both direct (e.g.
279 extraction of volcanic glass) and indirect (e.g. magnetic signals) approaches. Here the
280 method proposed by Turney et al. (1997), Turney (1998) and Blockley et al. (2005) was
281 employed, involving a stepped density separation using the inert heavy liquid sodium
282 polytungstate (SPT). Firstly a 'cleaning' float (specific gravity of 1.98 g $cm.^{3}$) is
283 performed to remove organics and diatoms, and then an 'extraction' float (specific
284 gravity of 2.55 g $cm.^{3}$) is carried out to separate the tephra shards from the heavier
285 minerogenic material. The published methods are deliberately flexible, allowing the
286 analysed grain-size and the separation densities to be tailored to the host sediment
287 type and expected volcanic ash characteristics. We chose to follow the recommended
288 separation densities, which have been carefully tested by Blockley et al. (2005) to show
289 optimal extraction of the majority of tephra shards encountered within several
290 European volcanic sources (e.g. Icelandic, Italian and Eifel). If present in the VIL core,
291 basaltic glass shards with a higher specific gravity than the SPT extraction density, were

292 not lost, but instead were retained in residues for inspection after the main float was counted. We

293 chose to analyse the sediment fraction between 125µm and 15µm. This is a wider size

294 range than the 80 - 25µm fraction most commonly used for cryptotephra (Blockley et

295 al., 2005), reflecting the uncertainty about the volcanic sources able to transport

296 tephra to NE Iberia. Smaller grain-size fractions are commonly used to maximise shard

297 numbers in this way (e.g. Kuehn and Froese, 2010), particularly where sites are very

298 distal from volcanic sources and their typical dispersal axes.

3.4. Single –grain quartz OSL and polymineral fine-grain IRSL

300 Fourteen luminescence dating samples were collected from unopened sections of the VIL

301 core and from some previously opened sections that had remained wrapped and

302 stored in a cold room since field recovery (Tables 4 and 5). Two luminescence dating

303 techniques have been used on these samples: i) five samples were dated at the Universidad Autónoma de Madrid's commercial dating laboratory using the

304 infrared stimulated luminescence (IRSL) signal from polymineral (mixed mineralogy) fine-grains (i.e. silt-sized grains)

305 and ii) nine samples were dated at the CENIEH laboratories (Burgos, Spain) using

306 the OSL signal from single-grains of quartz.

307 The results of the IRSL study have been already published (Moreno et al., 2012; González-

308 Sampériz et al., 2013) and are only summarised briefly in the current study. The single-

309 grain results were obtained by our own research team as part of the present dating

310 study, and are presented for the first time here. In both cases, the most homogeneous

311 silt or sand-sized layers were sampled in order to minimise uncertainties in gamma

312 dose rate estimation. Blocks of 5-15 cm vertical length were cut from 60 cm-long core

313 sections using a knife and wrapped in light-proof bags for transportation. Coarse-

314 grained (212-250 µm or 180-250 µm) quartz and fine-grained (2-10 µm) polymineral

315 fractions were prepared for OSL and IRSL burial dose estimation, respectively, using

316 standard procedures (Aitken, 1998). A 48% (40 min) hydrofluoric acid (HF) etch was used to

317 remove the alpha-irradiated external layers of the sand-sized quartz grains. The HF-etched quartz fractions were treated with concentrated (30%) hydrochloric acid (1 hour duration) to remove any fluoride precipitates, and subsequently re-sieved using a 90 µm sieve to remove any remaining (partially etched) feldspars and smaller disaggregated quartz grains.

318 IRSL measurements of the polymineral fine-grained material were made using a Risø TL-DA-10 reader

319 equipped with IR LEDs and a calibrated 90Sr/90Y beta source. Equivalent dose (De) estimates were determined from ultraviolet emissions using a multiple aliquot additive dose (MAAD) protocol and a preheat of 180 oC for 10 s prior to an IRSL stimulation for 120 s at 50oC. Further procedural details

320 for these previously published results are given in the Appendix.

321 For the single-grain OSL dating approach applied to coarse-grained quartz De values were estimated

322 from the ultraviolet emissions using the same

323 instrumentation, single-aliquot regenerative-dose (SAR) protocol (Murray and Wintle,

324 2000), and associated grain rejection criteria described in Arnold et al. (2012, 2013). Specifically, individual grain De estimates were rejected from further consideration if they exhibited one or more of the following properties: (i) weak OSL signals (i.e. the net intensity of the natural test-dose signal, Tn, was less than three times the standard deviation of the late-light background signal); (ii) poor recycling ratios (i.e. the ratios of sensitivity-corrected luminescence response (Lx/Tx) for two identical regenerative doses were not consistent with unity at 2σ); (iii) high levels of signal recuperation (i.e. the sensitivity-corrected luminescence response of the 0 Gy regenerative-dose point amounted to more than 5% of the sensitivity-corrected natural signal response (Ln/Tn) at 2σ); (iv) contamination by feldspar grains or inclusions (i.e. the ratio of the Lx/Tx values obtained from two identical regenerative doses measured with and without prior IR stimulation (OSL IR depletion ratio) was less than unity at 2σ); (v) saturated or non-intersecting natural OSL signals (i.e. Ln/Tn values equal to, or greater than, the Imax saturation limit of the dose-response curve); (vi) extrapolated natural OSL signals (i.e. Ln/Tn values lying more than 2σ beyond the Lx/Tx value of the largest regenerative-dose administered in the SAR procedure); (vii) anomalous dose-response curves (i.e. those displaying a zero or negative response with increasing dose) or dose- response curves displaying very scattered Lx/Tx values (i.e. those that cannot be successfully fitted with the Monte Carlo procedure and, hence, do not yield finite De values and uncertainty ranges).

325 Single grains were optically stimulated using a focussed 10 mW green (532 nm) laser

326 for 2 s at 125°C. Sensitivity-corrected dose-response curves were constructed using the

327 first 0.08 s of each green laser stimulation after subtracting a mean background count

328 obtained from the last 0.25 s of the OSL signal. De uncertainties were derived from net

329 photon counting statistics, an empirically determined instrument reproducibility of

330 1.8% per OSL measurement (calculated for the Risø reader used in this study), and a

331 dose-response curve-fitting uncertainty determined using 1000 iterations of the Monte
332 Carlo method described by Duller (2007) (implemented in Analyst v3.24). A preheat of
333 200 oC for 10 s was used in the SAR procedure prior to measuring the natural- and
334 regenerative-dose OSL signals. A preheat of 160 oC for 10 s was applied prior to each
335 test dose OSL measurement. Single-grain dose-recovery tests performed on V127
336 yielded measured-to-given dose ratios consistent with unity (0.96 ± 0.03; n = 83 De values) and a
337 relatively low over-dispersion value of 11 ± 4%, confirming the suitability of the chosen
338 SAR measurement conditions for single-grain De estimation.
339 Environmental dose rates were calculated for the single-grain OSL samples using high-
340 resolution gamma spectrometry measurements made with high-purity Ge detectors
341 (an n-type closed-end coaxial system and a p-type well system) (see SI for further
342 details). To estimate the long-term water content of the single-grain OSL samples we
343 have used the 'as measured' values and included a correction to account for
344 progressive decreases in sediment porosity with time. This correction has been
345 included because of the relatively thick sediment overburdens (27-73 m) affecting
346 these samples and, hence, the increased likelihood of sediment compaction and
347 dewatering effects with time (e.g., Rendell, 1985; Sheldon and Retallack, 2001; Olley et
348 al., 2004a, Kadereit et al., 2012; Lukas et al., 2012; see Table 1 and SI for further
349 details).
350 3.5. Paleomagnetism
351 Due to the fact that the VIL core is not oriented, only the paleomagnetic inclination can be
352 considered (not declination). In addition, it is expected that the paleomagnetic
353 declination is similar for the samples of the same section if the calculated stable
354 paleomagnetic component is primary; i.e., if it is acquired at the time of deposition of
355 the sediments (detrital remanence magnetization DRM). For the last normal chron
356 (Bruhnes chron, ~780 ka, v) up to 5 excursions of the magnetic field occurred
357 (Channell, 2006), and one of them – the Blake excursion ~120 ka - has been recently
358 radiometrically dated in a Northern Spain speleothem between 112 and 116.5 ka
359 (Osete et al., 2012). Consequently, to better constrain the basal age of the VIL sequence,
360 we focused the paleomagnetic study in the interval where the preliminary dating
361 (Moreno et al., 2012) suggested the 120 ka horizon occurs. Thirty three samples were

362 taken every 10 to 20 cm along the selected depth interval by cutting the halfcore with

363 a ceramic knife in cubes of 2 cm. The analyses were carried out at the Paleomagnetism

364 Laboratory of the University of Burgos, Spain. A 2-G cryogenic instrument with automated

365 alternating field (AF) demagnetization coils were used to measure the remanence and to

366 carry out the stepwise demagnetization procedure, respectively. Three samples were

367 thermally demagnetized but results were good in the AF demagnetization, therefore,

368 the AF demagnetization procedure was preferred. The calculation of the

369 paleomagnetic components was done with Remasoft (Chadima and Hrouda, 2009),

370 which follows the principal component analyses of Kirschvink (1980).

371

372 4. RESULTS

373 4.1. Radiocarbon (AMS 14C)

374 Seven of the twenty three AMS ages show reversals or outlier ages compared to the

375 preceding and subsequent samples (in italics in Table 2). The varied admixtures and origin of organic matter in the bulk sediment samples could explain some of these inconsistencies. Three of the samples, at 135, 638.2

376 and 989.5 cm depth (VIL05-1B-1T) have relatively higher algal organic matter content

377 as deduced from their relatively low TOC/TN ratios and d13C values (Table 2). This

378 feature could explain their relative age overestimates, as they could be more affected by

379 old carbon in the lake water reservoir (Geyh et al., 1998; Hou et al., 2012). The other four ages are inconsistent with the

380 general chronostratigraphy, but there was no clear a priori hypothesis to reject them. We ran an initial Bayesian model (details explained in the Discussion section below) to make the decision on which radiocarbon dates

381 were to be included in the final model and these seven samples giving reversed or outlier ages were excluded.

383 The final age radiocarbon model is therefore constrained by 16 AMS 14C ages for the upper 20 m of

384 the composite sequence.

385

386 4.2. U/Th

A number of problems, common when dating lacustrine carbonates by U/Th (Placzek et al., 2006 a) were encountered in the VIL sequence; finally, only three samples produced ages (VIL-2, -3 and -4; Table 3B). Firstly, even after long procedures, the amount of suitable material collected was too small, thus leading to higher uncertainty in the results. Secondly, carbonate-coatings are more difficult to clean than gastropod samples, and even after a very careful cleaning, the detrital 232Th concentration in all samples was very high. The 230Th/232Th ratio is only above 100 for VIL-3 and VIL-4 (Table 3B). This high detrital thorium content impeded the calculation of a meaningful age for samples VIL-1, VIL-5 and VIL-6 and produced a large associated uncertainty in sample VIL-2.

The uncertainties on the three dated samples (VIL-2, -3 and -4) are high, particularly for sample VIL-2, likely because of the high detrital content and the low sample weight. Potential variability in any assumed initial 230Th/232Th ratio is usually high in lacustrine samples because the proportion of ‘‘siliciclastic Th’’ and ‘‘unsupported Th’’ may not be constant (Placzek et al., 2006b). Therefore, age corrections using a constant initial 230Th/232Th ratio introduce larger errors, as reflected in the inaccuracies of the dated samples VIL-2, -3 and -4. Isochron techniques could probably help to obtain an age for these samples after initial 230Th/232Th ratio determination of the non-carbonate detritus. However, the requirement of obtaining multiple sub-samples with different degrees of contamination at the same core depth (same age) prevents the application of this methodology to the VIL core, particularly as it was difficult collecting sufficient material for just one sample at each depth.

The uppermost age (VIL-2) was rejected because it has the largest error and it is also stratigraphically reversed compared to the other two ages (VIL-3 and VIL-4). Thus, although six samples (endogenic and biogenic carbonates) were prepared and analysed, only two biogenic samples (gastropods) could be considered valid samples. Since these two samples (VIL-3 and VIL-4) were obtained close to the base of the core they could provide a basal age for the sequence, although the ages were much older (240 ka in U-Th) compared to the IRSL dates (140 ka, see below). Biological effects were considered responsible for this discrepancy, as one prerequisite for U/Th dating is a chemically -closed radioactive system, and this is unfortunately rarely the case for

418 biogenic carbonate due to chemical mobility of uranium, particularly during early diagenetic
419 stages (Placzeck et al., 2006a,b). Unfortunately, the absence of suitable material
420 impeded the use of the U/Th series techniques to correctly date the VIL sequence. However the basal age could serve as a maximum limiting age for the sequence.
421
422 4.3. Tephrochronology
423 Cryptotephra studies from Europe and the North Atlantic have shown that small
424 concentrations of volcanic ash can be found over several thousands of km away from
425 their source (Lane et al., 2017), therefore we expected some volcanic ash in El Cañizar
426 de Villarquemado. However, only a few tephra shards (<5 shards per gram) at two
427 intervals (5.90-6.00 and 12.30-12.50 m depth) were detected under high powered
428 optical microscopic analysis of the extracted residues within the depth interval 4-23m.
429 Despite extensive efforts, however, these could not be replicated at higher 1 cm
430 resolution and thus neither their integrity as primary ash fall layers could be confirmed
431 nor geochemical analyses carried out (Figure 4). These results are similar to other
432 recent attempts from paleo-archives across the Iberian Peninsula (Sanabria, Estanya;
433 unpublished data) where no cryptotephra were detected or, samples yielded minimal
434 evidence of tephra input and were insufficient for geochemical analysis.
435 Tephra occurrences in Late Quaternary Iberian records are rare and seem restricted to
436 Early Holocene volcanic activity in La Garrotxa region, Northeastern Spain (Höbig et al.,
437 2012; Bolòs et al., 2015). Volcanic ash could reach the Iberian Peninsula from several
438 sources: the Azores islands to the west, the Iceland to the north and Massif Central
439 and Italian volcanic systems to the East, all of which were active and generated far-
440 travelled tephra deposits during the last glacial cycle.
441 The most likely reason that ash from northern and eastern volcanic sources did not
442 reach Iberia is because the atmospheric circulation patterns were dominated by a
443 strong westerly and Northwestern component during the Last Glacial period (Moreno et al.,
444 2005), as they are today (Barry and Chorley, 1992). This essentially blocks atmospheric
445 transport paths required for transport of ash from East to far West. In fact, during the
446 last 2010 Icelandic Eyjafallajökull volcano eruption (Stevenson et al., 2012), only small
447 size volcanic particles were detected in Iberia (Revuelta et al., 2012) and no relevant

ash particles deposited.

It is unclear why volcanic ash from the Azores volcanic system, located around 2000 km to the west of El Cañizar de Villarquemado and highly active during the Last Glacial with multiple caldera-forming eruptions (Moore, 1990), has not been found yet in any Iberian lake sequence. One aspect that deserves further study is the role of precipitation and aridity in tephra deposition dynamics, as periods of higher aridity and varied vegetation cover during the Last Glacial Cycle in Iberia (García-Ruiz et al. 2003; González-Sampériz et al. 2010; 2017; Moreno et al., 2012; Sancho et al., 2018), may have significantly reduced the potential for tephra deposition and preservation. Another possibility is that grain size of the volcanic particles reaching Iberia may be too small to have been detected with our techniques. Tephra grain size distributions distal to source are controlled by factors including the volume of material ejected during the explosive phase of an eruption, the timing and extent of magma fragmentation and processes of aeolian fractionation during atmospheric transport. Iberia lies several hundreds of km away from most explosive volcanic regions. The 2010 Eyjafallajökull eruption was less explosive than many Late Quaternary eruptions are believed to have been (Davies et al., 2010; Stevenson et al., 2015), however it provides evidence that some volcanic ash may reach Iberia, but only in very small quantities and size fractions. Within this investigation, 15µm was the smallest mesh size used, but if most tephra fall over Iberia falls within a much smaller particle size range, sieves with smaller mesh diameters may need to be employed in future cryptotephra investigations. This has non-trivial implications for both optically identifying tephra at these small sizes and acquiring geochemical data for characterisation: as the smallest electron microprobe beam size currently in use for glass analysis is 3µm (Haywood, 2012), whilst ~10 µm is more common (Kuehn et al., 2011).

Whilst cryptotephrochronology was not successful in the VIL sequence, it is clear that to establish the absence or presence of non-visible ash layers in other areas of Iberia, requires a more comprehensive assessment of a larger number of Late Quaternary sediment sequences.

478 4.4. Paleomagnetism

479 The paleomagnetic results are shown in Figure 3. Samples demagnetized below 90 mT.

480 The natural remanent magnetization of all samples averages 6.2 10-4 A/m with a standard deviation

481 of 7.6 10-4 (Figure 3a). In 23 samples out of 33, two stable components can be calculated,

482 one that demagnetized between 2 and 16 mT (3-7 steps), and the component that

483 directs towards the origin (characteristic) and demagnetizes between 10-30 and 40-90

484 mT (4-19 steps) (Figures 3b to 3e). These two components can be calculated in the

485 coarser facies (grey silts and brownish sands) but not in the black clays (Figure 3d). The

486 viscous component groups in a northerly and normal component, probably due to

487 acquisition of the present day magnetic field during storage. The characteristic

488 component shows normal and reverse polarities in almost all sections (not in 103, 106

489 and 109 due to low number of samples), but the declination is not similar among the

490 samples from the same section (or antipodal in the case of opposite polarity, Figure 3f).

491 Therefore, a secondary stable remanent magnetization was acquired after deposition

492 of the sediments, maybe during coring extraction. Diagenetic redox reactions may

493 have also imprinted a secondary polarity as post-sedimentary magnetization can occur

494 (Roberts, 2015 and references therein). This could have been the case for the black

495 clays, with very low NRM and unstable paleomagnetic behaviour, due to the

496 destruction of ferromagnetic minerals by redox reactions in more organic matter-rich

497 sediments.

498 To sum up, paleomagnetic studies could not identify the normal polarity expected for the samples and particularly it was not possible to detect the reverse polarity associated to the Blake excursion (~120 ka) that was anticipated to be found within the lower interval of the sequence. We do not have a valid explanation for this, since at sample level, a stable characteristic magnetic component was calculated (for most samples), but at section level, it was not possible to define local magnetozones.

500

501

502 4.5. Single-grain OSL and polymineral fine-grain IRSL results

503 Polymineral fine-grain IRSL results

504 The previously published IRSL ages for the five VIL samples are summarised in Table 4.

The previously published IRSL ages for the five VIL samples are summarised in Table 4. Multiple aliquot storage tests conducted on a subset of these samples by Universidad Autónoma de Madrid suggest that the polymineral fine-grain IRSL signals may not be significantly affected by anomalous fading; signal losses were reported to be <3% and within analytical uncertainties following storage times of 240 h (n = 4 aliquots per measurement); though further details of the procedures adopted in these fading assessments are unavailable. Anomalous fading of polymineral IRSL signals has been shown to be a near ubiquitous problem across a wide range of geological provinces (Wintle, 1973; Aitken, 1985, 1998; Huntley and Lamothe, 2001), particularly when employing De estimation procedures that include low preheat temperatures (180 oC for 10 s) and measurement of ultraviolet rather than blue IRSL emissions (e.g., Clarke and Rendell, 1997; Preusser, 2003). As such, we cannot preclude the possibility of minor age underestimation arising from unaccounted fading with the polymineral fine-grain IRSL results. It would be worth conducting additional fading tests on these sample using different sized laboratory doses, multiple delay times and signal sensitivity-correction procedures (e.g., Auclair et al., 2003 and Huntley and Lamothe, 2001). Irrespective, the polymineral fine-grain IRSL ages are in stratigraphic order and the age of sample MAD- 5172SDA (40.4 ± 3.4 ka) is in good agreement with two bracketing AMS 14C ages of 36.3- 40.2 ka and 40.2-42.9 ka (Table 5), providing support for the general suitability of the IRSL datasets.

520 Single-grain quartz OSL results

521 Table 5 and Figure 4 summarise the single-grain De estimates, dose rate data and final

522 ages obtained for El Cañizar de Villarquemado samples. The specific activities of 40K and

523 individual isotopes in the 238U and 232Th series are also shown in Table 6.

524 Isotopic ratios for 226Ra/238U, 210Pb/226Ra and 228Th/228Ra are consistent with unity at 1s

525 or 2s for all nine samples, indicating that the 238U and 232Th decay chains of these

526 sediments are within analytical uncertainty of present-day equilibrium. To calculate

527 the optical ages of these samples, we have assumed that present-day equilibrium in

528 the 238U and 232Th decay chains has prevailed throughout the burial period.

529 Between 900 and 1300 individual quartz grains were measured per sample (Table 5)

530 and 6-9% of these grains were considered suitable for De determination after applying

531 the single-grain quality assurance criteria outlined in Arnold et al. (2013). The vast majority of measured grains were rejected for having weak OSL signals (50-60% of measured grains per sample) and anomalous / scattered dose-response curves (15-30% of measured grains per sample), with the remaining rejection criteria each accounting for less than 5% or 10% of measured grains per sample. The De distributions of these samples can be broadly grouped into two categories. Samples

533 V67, V127, V135 and V148 display homogeneous single-grain De distributions,

534 characterised by relatively limited De scatter (e.g., Figure 5b). These De datasets are

535 consistent with a single dose population centred on the weighted mean De value and

536 display relatively low over dispersion values of ~13-22% (Table 5). These

537 overdispersion values are consistent with the average value of ~20% commonly

used to interpret samples as well-bleached and unaffected by post-depositional mixing or significant beta-dose spatial heterogeneity (e.g., Olley et al., 2004a; Arnold and Roberts, 2009, Arnold et al., 2011). The overdispersion values of these samples also overlap at 2s with the over-dispersion value obtained in the single-grain dose-recovery test (11 ± 4%). The consistency of these results suggests that intrinsic sources of De scatter captured by the dose-recovery test likely account for the natural De distribution characteristics of these four samples and that extrinsic De scatter is relatively unimportant. We have therefore estimated the final burial doses for these samples from their weighted mean De estimates, calculated using the central age model (CAM) of Galbraith et al. (1999).

Samples V49, V58, V99, V110, V117, display broader De ranges (e.g., Figure 5c) and a significant proportion of the individual De values are not consistent with the sample-averaged (CAM) burial dose estimates at 2s. The overdispersion values for these samples range between 26% and 37% and do not overlap at 2s with the corresponding overdispersion value obtained for either the single-grain dose-recovery test or the 'best-case scenario' natural De distribution observed in the VIL core ((i.e., the natural De distribution with the lowest overdispersion value in this sample dataset = sample V127: overdispersion = 13 ± 3%, suggesting that dose dispersion originating from extrinsic, field-related sources is more significant. The radial plots also display distinct 'leading-edges' of low De values and / or elongated, asymmetric 'tails' of higher De values, as has been commonly reported for partially bleached single-grain De distributions (e.g., Olley et al., 1999; 2004a; Bailey and Arnold, 2006; Arnold et al., 2007, 2009). Taking into account these empirical De characteristics, the alluvial and sub-aqueous origin of these deposits, and the potentially limited transportation distances experienced prior to deposition in this closed basin, it seems feasible that the additional De scatter may be primarily attributable to insufficient bleaching at the time of deposition; though minor dose dispersion arising from other extrinsic sources of De scatter (e.g., beta dose heterogeneity) cannot necessarily be discounted. Post-depositional mixing is not thought to have contributed significantly to the De scatter of these samples because primary sedimentary structures and distinctive boundaries are preserved through the sampled region of the core profile. In light of these considerations, the burial doses of samples V49, V58, V99, V110 and V117 have been determined using the 4-parameter

569 minimum age model (MAM-4) of Galbraith et al. (1999). Further support for this choice

570 of age model comes from the accuracy of the MAM-4 OSL age obtained for V49 (49 ± 8

571 ka). This OSL age is consistent with the expected age range of Unit IV based on an

572 overlying 14C sample (40.2-42.9 ka) and lithostratigraphic correlations of these deposits

573 with MIS 3 (57-29 ka; Lisiecki and Raymo, 2005; Moreno et al., 2012). In contrast, the

574 CAM age for V49 (79 ± 8 ka) is significantly older than the expected age range of Unit

575 IV, consistent with the interpretation that this sample was poorly bleached prior to

576 deposition.

The reliability of the single-grain OSL De estimates obtained in this study partly depends on whether the accepted grain populations have sufficiently high dose saturation limits to ensure finite De estimation over the true natural burial dose ranges of interest; particularly as the measured De values of the Villarquemado samples typically exceed 100 Gy. To examine whether our single-grain OSL De results have been compromised by dose saturation, we analysed the characteristic saturation dose (D0) values of accepted grains for the various coarse-grain quartz samples. Figure S1 shows the range of single- grain quartz OSL D0 values obtained for accepted grains from a representative luminescence dating sample (V127); similar trends were observed for all other samples in this study. The weighted mean (CAM) D0 value for the combined accepted grains of sample V127 (n = 81) is 218 ± 11 Gy (Figure S1), with the majority of accepted grains (>80%) exhibiting individual D0 values in excess of 200 Gy. These D0 values are higher than those typically reported for single-grain quartz OSL datasets (see overview and discussions in Arnold et al., 2016), and sufficiently high to enable finite De determination over the empirical burial dose ranges of the Villarquemado samples (Table 5, Figure 4). As such we do not consider that the single-grain OSL ages have been negatively affected by dose saturation. To explore this issue further, we applied the 2 × D0 acceptance threshold criterion outlined by Demuro et al. (2015, 2019), which ensures that only grains with 2 × D0 values higher than a specific burial dose are accepted for final De estimation. This additional quality assurance criterion is designed to eliminate grains that produce unrealistically low De values purely as a result of insufficient dose saturation limits, thus avoiding potential age underestimation arising from inherently unsuitable grains. Progressively higher 2 × D0 thresholds of 150 to 800 Gy (increasing in 50 Gy increments) were applied to all the samples, and the effects on weighted mean De were examined after taking into consideration associated 2σ uncertainty ranges (see details in Arnold et al., 2016). For all nine single-grain OSL samples, it was found that selecting grains with progressively higher D0 values did not result in significantly higher CAM De values (Figure S2). Instead, both the CAM De and overdispersion remained within 2σ of the original values shown in Table 5. These results indicate that the original single-grain OSL ages calculated using all accepted grains have not been adversely affected by OSL dose saturation.

577 Integration of polymineral fine-grain IRSL and single-grain quartz OSL ages

578 The nine single-grain OSL ages are internally consistent and in correct stratigraphically

579 order, providing additional support for our age model selection procedure. The single-

580 grain quartz OSL ages and polymineral fine-grain IRSL ages are also in broad agreement with each

581 other at their 1s or 2s error ranges, and provide a stratigraphically consistent

582 combined chronological dataset. There are signs of an emergent systematic deviation between the single-grain quartz OSL ages and polymineral fine-grain IRSL ages over the lower 15 m of the core (between a depth range of 59-74 m), though the two chronological datasets remain statistically indistinguishable at 2σ. The general age agreement between the polymineral fine-grain IRSL and single- grain quartz OSL methods is somewhat unexpected for at least some of these samples (i.e., samples V49, V58, V99, V110 and V117) given that they show evidence of prominent single-grain De scatter that appears to be related to partial bleaching. The complicating effects of partial bleaching cannot be directly evaluated for the polymineral fine-grain IRSL datasets as the measured aliquots contain 105-106 grains, and therefore give rise to homogenised (grain-averaged) De values (e.g., Arnold and Roberts, 2009; Arnold et al., 2013). Any resultant age overestimations associated with such polymineral IRSL averaging effects may not be apparent in the present study if opposing biases have acted to mask the effects of insufficient bleaching (e.g., polymineral IRSL age underestimation related to anomalous fading that has gone undetected in the existing laboratory assessments, or absence of a suitable overburden compaction correction procedure in the previously published IRSL study; see Supplementary Material for discussions of luminescence dating sensitivity to the compaction correction procedure). However, given the apparent agreement of the polymineral IRSL and single-grain OSL ages, and the difficulties of directly demonstrating that the IRSL ages have otherwise been compromised by compensatory biasing effects, we consider both luminescence datasets to be valid for Bayesian age-depth modelling purposes. That said, we place greater emphasis on single-grain OSL quartz ages generated in the present study because: (i) quartz OSL signals bleach more rapidly than feldspar IRSL signals (e.g., Godfrey-Smith et al., 1988) and therefore offer advantages for some of the deposits that could have experienced limited / filtered bleaching spectra prior to deposition; (ii) fast-dominated quartz OSL signals (i.e., those typically isolated with SAR De measurement procedures) are not compromised by athermal signal instabilities, unlike many IRSL signals measured at low (50oC) stimulation temperatures (e.g., Huntley and Lamothe, 2001); (iii) De determination at the single-grain scale of analysis circumvents any potentially complicating grain-averaging effects (e.g., Demuro et al., 2008, 2013; Arnold et al., 2012), and enables any subpopulations of poorly bleached grains to be identified and examined with appropriate statistical approaches prior to final age calculation; and (iv) the single-grain quartz OSL ages have been derived using a more thorough consideration of long-term changes in sediment water contents.

691

608 5. DISCUSSION

609 5.1. A Bayesian approach for El Cañizar de Villarquemado Age-Depth Model

610 5.1.1. Previous chronologies

611 Since the 2005 core extraction, several attempts have been made at modelling a

612 robust independent chronology for the VIL sequence. The first model included nine AMS

613 14C ages and five IRSL ages (Moreno et al., 2012). This age model was developed using
614 linear interpolation between all of the radiocarbon and IRSL ages. The base of the
615 sequence was established at ca. 120 ka, with large basal age errors (ca. 10 ka). The
616 robustness of this age model was strengthened by the coherence between the AMS
617 14C age at 1912 cm (40.2 – 42.9 ka) and the IRSL age at 1832 cm (40.4 ± 3.4 ka).
618 A second age model (González-Sampériz et al., 2013) added three more AMS 14C ages
619 (twelve in total) for the top 20 m depth and was constructed following Heegaard et al.,
620 (2005). The time resolution for the Holocene improved but remained similar for the
621 previous intervals. According to this second model, the base reached 130 ka and the
622 boundary between MIS 6 and MIS 5 was tentatively located at the base of sedimentary
623 unit VII (74 m depth), while MIS 4 was identified in sedimentary unit V (37-29 m depth)
624 and MIS 3 comprised sedimentary units IV, III and the main part of II (29-5.5 m depth).
625 Sedimentary unit I (top 2.5 m) represented MIS 1. Aranbarri et al. (2014) included four
626 new AMS 14C ages (1 from the long core and three more from the parallel core VIL05-
627 1A) for the Holocene age model.
628
629 5.1.2. A Bayesian approach
630 To build an integrated age model we could only use ages obtained from three of the
631 different techniques originally employed: AMS radiocarbon, IRSL and OSL. As discussed
632 earlier, the only available U/Th dates were too old, likely as the biogenic carbonate
633 system did not remain chemically closed, and the paleomagnetic studies could not
634 determine a consistent reverse polarity in the lower interval of the sequence that
635 could be related to the Blake excursion (~120 ka). Cryptotephra techinques did not provide suitable material for dating either.
636 Preliminary age models clearly showed a lack of linearity in the age-depth relationships
637 (Moreno et al., 2012; González-Sampériz et al., 2013; Aranbarri et al., 2014). This is a
638 common feature in terrestrial sequences, where, very often, calibrated radiocarbon
639 ages exhibit non-gaussian probability distributions. Taking into consideration the discussion of the validity of the different data sets from the previous section, we decided to combine the
640 sixteen AMS 14C ages, the five previously published IRSL ages and the nine single-grain
641 OSL ages into a new Bayesian modelling framework (Blockley et al., 2008; Ramsey,
642 2009; Blaauw and Christen, 2011; Hogg et al., 2011; Goring et al., 2012). The rationale

643 behind this method implies building up a depositional model taking into account the well-known depth (and hence also, by inference, the relative age) relationships between samples used for dating.

Of particular significance for lake sequences is the fact that

645 the accumulation process can be modelled by considering that the deposition rate at

646 every depth is a weighted average of the previous depths (Blaauw and Christen, 2011).

647 We have used Bacon v. 2.2 (Blaauw and Christen, 2011) for modelling purposes, which

648 additionally incorporates radiocarbon age calibration using the INTCAL13 curve

649 (Reimer et al., 2013).

650 Bacon controls core accumulation rates using a gamma autoregressive semi-

651 parametric model with an arbitrary number of subdivisions along the sediment. This

652 implies adding some prior knowledge on the evolution and shape (a) of accumulation

653 rates, which serves as a smoothness factor for the age series, followed by a self-

654 adjusting Markov Chain Monte Carlo (MCMC) process in order to build up a robust-to-

655 outliers age model. The latter involves an adaptive algorithm that learns about the

656 modelled process to automatically tune the MCMC simulation (Blaauw and Christen,

657 2011). Thus, the model includes as a pre-requisite the known fact that different

658 sections of a sequence have different accumulation rates. This means that low

659 variation in the accumulation rates throughout the deposit implies a high “memory”,

660 or internal dependence amongst sections of the sequence. Therefore, this procedure

661 demands the input of the mean expected accumulation rate (ß) and the prior for the

662 variability of accumulation rate, or “memory”. Additionally, it is necessary to define

663 the number of sections of the core in which the MCMC process will be repeated.

664 As in most long sequences, we lack precise a priori information on the accumulation

665 rate of the sequence and, given the length of the sequence and the variability in

666 sedimentary facies, building up a chronological model becomes challenging as the

667 sedimentation rate will have certainly changed through the sequence. Therefore, to

668 find the best set of priors to build the most suitable age-depth model for the VIL core,

669 we carried out a sensitivity analysis (see Supplementary material for details on this

670 method). From this analysis our parameters were set as follows: the number of

671 divisions in VIL sequence was 30, which implies that the MCMC process is roughly

672 renovated every 250 cm and that the variability of the sedimentation process is

673 relatively high (memory strength = 1 and mean correlation of 0.5). We set our prior for

674 the accumulation rate as a gamma distribution with shape 1 (a) and mean 30

675 (accumulation rate=30 yr cm-1). The definitive age model for the VIL (Figure 7) includes

676 thus the 16 available AMS 14C, IRSL and OSL ages, and considers the facies fluctuations

677 along the sequence, especially the changes occurring between sedimentary units VI

678 and V (38 m depth) and between sedimentary units V and IV (29 m depth).

The VIL sequence shows main depositional/vegetational changes and intervals that can concur with the boundaries of the last 6 Marine Isotopic Stages (Shackleton et al., 2002; Lisiecki and Raymo, 2005; Rasmussen et al., 2014) 838 Therefore, according to our age model, we define the following time periods:

74-72.3 m depth interval (132.,700-130,027 cal yrs BP corresponding), to the end of MIS 6.

72.3-38.3 m depth (130,027-71,011 cal yrs BP) coincident with MIS 5

38.3 -29.2 m depth (71,011-57,022 cal yrs BP) concurring with MIS 4

29.2-9.9 m depth (57,022-29,007 cal yrs BP) spanning MIS 3

9.9-3 m depth MIS 2 (29,007-14,043 cal yrs BP) corresponding to MIS 2

Upper 3 m depth (14,043 cal yrs BP – current times corresponding to MIS 1

Figure 5 shows the age – depth model for the VIL sequence. Accumulation rates were higher during cooler periods (end of MIS 6, MIS 5d, MIS5 b, MIS 4, MIS 2 onset and LGM) with average values ranging from 0.095 cm/yr at the end of MIS 6, to 0.053 cm/yr at MIS 2 onset and LGM. However, accumulation rates were also high, during MIS 3 when alluvial fans prograded into the lake basin and a

691 more open landscape perhaps also contributed to greater sediment input (Fig. Sed.

692 Rate changes, Appendix). On the contrary, during warm periods such as the Holocene

693 and MIS 5e, the sedimentation rate was much lower (between 0.022 and 0.057 cm/yr) since it was dominated by

694 autochthonous processes (eg. carbonate productivity in the lake) and a smaller

695 amount of sediment delivery from the catchment.

696

5.2. The evolution of El Cañizar de Villarquemado Lake basin during the last 135,000 years

The new age model allows the definition of the timing for the main environmental and hydrological changes reconstructed in the VIL sequence based on sedimentological, geochemical and palynological evolution identifies a number of large and rapid changes in the VIL basin during the last 135 ka (Figure 6). From a paleohydrological point of view, the development of carbonate lakes in the basin (facies association A in Figure 2, Table 1) represents periods of higher lake levels than during wetland stages, with higher TOC and lower MS. Alluvial fan deposits, with lower TOC content and higher MS, prograded during the periods with the lowest lake levels in the basin. Additionally, higher hydrophytes and hygrophytes fossil pollen content (aquatic taxa) as well as Pterydophyta spores (ferns), indicate periods of higher lake levels and/or wetlands development, thus, increased local moisture conditions in the basin (Figure 6). Accordingly, increasing percentages in steppe taxa identify arid conditions and lowest lake levels, while fluctuations in the Mediterranean component group are representative of temperature variability.

The age–depth model confirms that carbonate and peat-rich sediments (Figure 2, Table 1) were mainly deposited during the interglacials (Holocene and MIS 5), but also at the end of MIS 6, the beginning of MIS 4 and the second half of MIS 2 (Lateglacial). During these aforementioned phases we also find higher proportions of aquatic taxa pointing to increasing local moisture (Figure 6).

Presence of clastic lacustrine facies, low percentages of Mediterranean taxa and aquatics and increasing steppe taxa at the bottom of sedimentary unit VII (74 – 72 m depth, 132,700 – 129,661 cal years BP following our chronological model, thus end of MIS 6 and beginning of MIS 5), suggest that the base of the sequence corresponds to relatively cooler and drier climate conditions than afterwards. At a global scale, the age of Termination II is considered ca. 132-130 ka (Shackleton et al., 2002; Lisiecki and Raymo, 2005), although it has largely been a matter of debate (see literature review in Helmens 2014; Martrat et al., 2014; Sier et al., 2015). Similarly, the environmental responses were not synchronous over the European continent (i.e., Woillard and Mook, 1982; Guiot et al., 1989; Tzedakis et al., 1997, 2003; Kukla et al.,

727 1997; Allen and Huntley, 2009).

728 Based on our age model, the MIS 6 – MIS 5 boundary (ca. 130,027 ka) is located at 72.3 m

729 depth although it is at 70.3 m depth (127,566 cal yrs BP) when the first carbonate lake was

730 established (facies association A in Figure 2). The signature of interglacial conditions in

731 the VIL sequence after the onset of MIS 5 (Figure 6) was characterized by a trend towards warmer

732 conditions but still relatively low effective moisture, as reflected both in the

733 depositional processes and vegetation responses. This is indicated by the development of a

734 shallow carbonate lake and the lowest proportions of local moisture vegetation

735 formations within MIS 5, and the highest values of steppe taxa (Figures 2 and 6) with two maximum peaks dated at 128.5 and 127.2 ka BP following our chronological model.

736 After these maxima, a general decrease in steppe taxa is evidenced since ca. 126.9

737 ka (MIS 5e). In parallel, local moisture indicators developed in the

738 basin since ca. 125.2 ka. However the Mediterranean component presents the same

739 values along the MIS 6 – MIS 5 boundary (González-Sampériz et al., 2013; García-

740 Prieto, 2015).

741 Interestingly, a similar palynological scenario where neither rapid changes nor clear shifts occur regarding regional vegetation (mainly conifers and Mediterranean taxa) has been identified for the Last Termination

742 and the beginning of the Holocene (Aranbarri et al., 2014) (Figure 6). Thus, the absence

745 of significant changes during the Terminations in this record has been interpreted as a

746 signature of the resilient character of vegetation in Mediterranean continental Iberia

747 (González-Sampériz et al., 2013, 2017; Aranbarri et al., 2014; García-Prieto, 2015).

748 Detailed facies analyses of the MIS 5 interval in the VIL sequence - Units VII and VI in VIL, up to 38 m depth

749 and until 70.633 cal yrs BP - show seven major lacustrine carbonate - peat cycles covering the

750 whole of MIS 5. The lacustrine facies are charophyte-rich sand and silt, banded to

751 laminated grey silt, and variegated, bioturbated, mottled carbonate mud and silt

752 (Table 1, Figure 2). Those cycles are well marked too by TOC rich intervals 1 to 7

753 (Figure 6). The three oldest cycles dated at ca. 129, 125 and 114 ka BP following our chronological model, are dominated mainly by carbonate lake

754 environments in the basin, and suggest deeper lake levels compared to wetland depositional environments. This

755 humid phase in our record would correspond with MIS 5e (ca. 127-112 ka, Figure 6) in

756 agreement with the most humid period recorded in Monticchio between 127.2-109.5

757 ka and interpreted as the Eemian by Allen and Huntley, (2009). The higher development of carbonate-rich

760 facies in the VIL sequence at this moment would suggest a warmer and more humid

761 Eemian than the Holocene in this region (Aranbarri et al., 2014; Garcia-Prieto,

762 2015). This is consistent with global patterns of warmer and moister climate conditions of the Eemian (Sánchez-Goñi et al., 1999, 2000, 2005; Tzedakis et al., 2001) and for most reconstructions on mid latitude areas (van Andel and Tzedakis

763 1996; Magri and Tzedakis, 2000; Andersen et al., 2004; Dahl-Jensen et al., 2013; Lunt

764 et al., 2013; Otto-Bliesner et al., 2013; Bakker et al., 2014).

765 The second half of MIS 5 recorded at VIL is characterized by a larger development of wetlands and less

766 frequent carbonate lake environments, illustrating a trend towards relatively lower

767 humidity (Figure 2), although pollen indicators show a similar composition of main

768 vegetation groups including large local moisture fluctuations (Figure 6). Besides the

769 three oldest TOC rich intervals already mentioned corresponding with MIS 5e, we identify one during

770 MIS 5c (interval number 4, ca 95 ka BP) and the last three (5, 6 and 7: ca. 83, 78 and 73 ka BP, respectively, following our age model: Figure 6) during MIS 5a.

771 Similarly, higher proportions of Mediterranean taxa are also recorded in interstadials

772 MIS 5c and MIS 5a, and interglacial MIS 5e, pointing to higher temperatures (Figure 6).

773 The onset of Unit V (38.3 m, 71 ka) witnessed a significant depositional change in the

774 basin, as wetlands started to recede while distal alluvial fans prograded over the

775 central areas of the basin. The Mediterranean taxa disappeared (last peak occurred at 70.4 ka BP following out age model), suggesting colder

776 climate conditions but local moisture pollen indicators still record moderate values

777 (Figure 6). Our age model dates this transition as 71 ka corresponding with the onset of MIS 4 (Lisiecki and Raymo, 2005). At a regional scale (NE Iberian Peninsula), the transition from MIS 5 to

779 MIS 4 was marked by colder conditions but humidity remained relatively high

780 (González-Sampériz et al., 2010 and references therein), consistent with maximum

781 glacier extension in the northern Iberian mountains (Lewis et al., 2009; Sancho et al.,

782 2018).

783 In the VIL sequence, the aridity trend that had started during MIS 4 reached a maximum

784 during the lower part of MIS 3 (Unit IV, 29.2-21 m depth, ca. 57,002-44,063 cal yrs BP). During this unit,

785 there is clear evidence for the lowest paleohydrological levels in the basin in the form

786 of red, oxidized, fine silt facies with pedogenic features (facies association D in Figure

787 2, Table 1). Strong arid conditions during the whole of MIS 3 (sedimentary units V, IV,

788 III and the bottom part of unit II: ca. 57-29 ka) are indicated by the highest steppe taxa

789 proportions and the lowest local moisture group percentages of the whole record

790 (Figure 6). Additionally, two of the four intervals with low pollen productivity or sterility

791 recorded in the VIL sequence (marked by shaded grey bands in Figure 6) are located in MIS

792 3, from ca. 50.1-43.1 and from 37.4-31.2 ka BP following out chronological model and they are the result of low pollen preservation

793 conditions suggesting subaerial exposure.

794 MIS 2 and the Lateglacial (9.9-3 m depth, ca. 29,007-13.708 according to our age model) are characterized by greater

795 environmental and climate variability as indicated by the diversity of sedimentary

796 facies (Figure 2). Clastic-dominated lakes and alluvial fans covered the VIL basin, but

797 evidence for subaerial exposure is not found during the first half of MIS 2 (Table 1 and

798 Figure 2). The LGM is characterized by another new low pollen productivity interval

799 between 4 and 5.5 m depth (22,328-16,085 cal yrs BP from our age model: Figure 6).

800 Deposition of clastic and carbonate silt facies during the Lateglacial suggest an increase

801 in the flooded area in the VIL basin and higher run off and sediment delivery. Steppe taxa

802 decreased and never again reached similar proportions to those of MIS 3. Inversely,

803 the aquatic taxa (local moisture group) developed, reaching the maximum values of

804 the whole sequence during the Lateglacial at 13,140 cal yrs BP following our chronological model (Figure 6). The Mediterranean component

805 slowly expands and only peaks after the first millennia of the Holocene (after 7490 cal yrs BP) (Aranbarri et al., 2014).

807 The Holocene onset at 11.7 ka was abrupt from a sedimentological point of view, with

808 the development of a carbonate lake (Figure 2) while terrestrial vegetation remained

809 resilient with no significant changes until ca. 9.5 ka (Aranbarri et al., 2014), as observed

810 in other inner Mediterranean regional sequences (González-Sampériz et al., 2017;

811 Morellón et al., 2018 and references therein). Both pollen and sedimentological facies

812 indicate that the most humid Holocene phase occurred between ca. 7.7-5 ka BP and was

813 characterized by the highest development of carbonate facies (Figure 2, Table 1), the

814 maximum spread of mesophytes, the expansion of mixed Mediterranean oak

815 woodlands with evergreen Quercus as dominant forest communities, and more

816 frequent higher lake level periods (Aranbarri et al., 2014). The return of shallow,

817 carbonate-wetland environments occur in conjunction with a decrease of mesophytes

818 (Aranbarri et al., 2014), consistent with the widely identified increasing aridity of the

819 Late Holocene in the Western Mediterranean (Jalut et al., 2009; Di Rita et al., 2018).

820

821 6. CONCLUSIONS

822 A multiple dating technique was implemented for the 72 m long VIL sequence,

823 including AMS radiocarbon, IRSL and OSL, U/Th, tephrochronology and

824 paleomagnetism. In spite of the absence of useful ages from some dating techniques, this type of

825 strategy is essential to maximize the chances of obtaining robust age models in

826 terrestrial sequences. The final Bayesian age model for the VIL sequence includes 16 AMS

827 14C age, 5 previously published IRSL ages and 9 single-grain OSL ages. We did not find adequate

828 material for some analyses (U/Th, tephrochronology) and other

829 techniques did not provide reliable results (paleomagnetism). The Bayesian approach

830 improved the accuracy and resolution of the age-depth model by incorporating

831 additional information related to the known age relationship between samples, and also related to changes in accumulation rate, as revealed by detailed

832 sedimentological analyses. The age model demonstrates large paleohydrological and

833 vegetation variability since the penultimate Termination, which is consistent with main

834 global climatic trends, despite some local idiosyncrasies derived from stronger continentality in higher altitude Mediterranean areas. Shallow carbonate lake and

835 wetland environments developed during the interglacials (Holocene and MIS 5), but

836 also at the end of MIS 6, the beginning of MIS 4 and the second half of MIS 2

837 (Lateglacial). Clastic lakes dominated during MIS 2 and MIS 4, and distal alluvial fans

838 prograded over the basin during MIS 3. Sedimentological, geochemical and

839 palynological data suggest that the Eemian was wetter and warmer than the Holocene at VIL.

840 The onset of MIS 4 was marked by cooler temperatures, although conditions

841 remained relatively humid until MIS 3, the most arid interval in the whole sequence.

842 MIS 2 shows large depositional and vegetation variability. The Holocene onset was

843 marked by an abrupt paleohydrological change, but the main terrestrial vegetation

844 change was delayed several millennia until 9.5 ka. This depositional and paleohydrological evolution

845 of the VIL lake during the last interglacial – glacial transition reveals higher moisture

846 variability than expected, an abrupt inception of the last glacial cycle and a resilient

847 response of vegetation in Mediterranean continental Iberia in both Terminations.

848

849 ACKNOWLEDGEMENTS

850 Funding for El Cañizar de Villarquemado sequence research was provided by

851 DINAMO (CGL-BOS 2009–07992), DINAMO2 (CGL-BOS 2012–33063), DINAMO 3

852 (CGL2015-69160-R) IBERIANPALEOFLORA (CGL-BOS 2012–31717) and GRACCIE-

853 CONSOLIDER (CSD2007-00067) projects, provided by the Spanish Inter-Ministry

854 Commission of Science and Technology (CICYT) and by the Aragon Government (DGA

855 project, 2005-2006). Tephrochronology research was supported by the UK Natural

856 Environment Research Council consortium RESET (NE/E015670/1). The single-grain OSL

857 dating research was supported by Australian Research Council (ARC) Future Fellowship

858 project FT130100195 and Discovery Early Career Researcher Award DE160100743.

859 The work of BMB was supported by the IGNEX project (249894), funded by the

860 FRIMEDBIO program of The Research Council of Norway. Graciela Gil-Romera is funded

861 by the DFG project FOR 2358 "Mountain Exile Hypothesis". We are grateful to two anonymous reviewers whose comments and suggestions improved the manscript.

862

863 DATA AVAILABILITY

Data for this research are available in Mendeley Data Repository

872 REFERENCES

873 Aitken, M. J., 1985. Thermoluminescence Dating. Academic Press, London, 359 p.

874 Aitken, M.J., 1998. An Introduction to Optical Dating: The Dating of Quaternary

875 Sediments by the Use of Photon-Stimulated Luminescence. Oxford University

876 Press, Oxford, 267 p.

877 Allen, J.R.M., Huntley, B., 2009. Last Interglacial palaeovegetation,

878 palaeoenvironments and chronology: a new record from Lago Grande di

879 Monticchio, southern Italy. Quaternary Science Reviews 28, 1521-1538.

880 Andersen, K.K., Azuma, N., Barnola, J.M., Bigler, M., Biscaye, P., Caillon, N., Chappellaz,

881 J., Clausen, H.B., Dahl-Jensen, D., Fischer, H. and Flückiger, J., 2004. High-

882 resolution record of Northern Hemisphere climate extending into the last

883 interglacial period. Nature 431, 147-151. Aranbarri, J., González-Sampériz, P.,

884 Valero-Garcés, B., Moreno, A., Gil-Romera, G., Sevilla-Callejo, M., García-Prieto,

885 E., Di Rita, F., Mata, M.P., Morellón, M., Magri, D., Rodríguez-Lázaro, J., Carrión,

886 J.S., 2014. Rapid climatic changes and resilient vegetation during the Lateglacial

887 and Holocene in a continental region of south-western Europe. Global and

888 Planetary Change 114, 50–65.

889 Arnold, L. J., Bailey, R. M., Tucker, G. E., 2007. Statistical treatment of fluvial dose

890 distributions from southern Colorado arroyo deposits. Quaternary

891 Geochronology 2, 162–167.

Arnold, L.J., Roberts, R.G., Macphee, R.D.E., Willerslev, E., Tikhonov, A.N., Brock, F. 2008.

1077 Optical dating of perennially frozen deposits associated with preserved ancient

1078 plant and animal DNA in north-central Siberia. Quaternary Geochronology 3, 114-

1079 136.

892 Arnold, L.J., Demuro, M., Navazo Ruiz, M., Benito-Calvo, A., Pérez-González, A., 2013.

893 OSL dating of the Middle Palaeolithic Hotel California site, Sierra de Atapuerca,

894 north-central Spain. Boreas 42, 285-305.

895 Arnold, L.J., Demuro, M., Navazo Ruiz., 2012. Empirical Insights into multi-grain
896 averaging effects from 'pseudo' single-grain OSL measurements. Radiation
897 Measurements 47, 652-658.
898 Arnold, L.J., Roberts, R.G., 2009. Stochastic modelling of multi-grain equivalent dose
899 (De) distributions: Implications for OSL dating of sediment mixtures. Quaternary
900 Geochronology 4, 204-230.
901 Arnold, L.J., Roberts, R.G., Galbraith, R.F., DeLong, S.B., 2009. A revised burial dose
902 estimation procedure for optical dating of young and modern-age sediments.
903 Quaternary Geochronology 4, 306-325.
904 Arnold, L.J., Roberts, R.G., MacPhee, R.D.E., Haile, J.S., Brock, F., Möller, P., Froese,
905 D.G., Tikhonov, A.N. Chivas, A.R., Gilbert, M.T.P., Willerslev, E., 2011. Paper II –
906 Dirt, dates and DNA: OSL and radiocarbon chronologies of perennially-frozen
907 sediments and their implications for sedimentary ancient DNA studies. Boreas
908 40, 417-445.
909 Arnold, L.J., Demuro, M., Parés, J.M., Pérez-González, A., Arsuaga, J.L., Bermúdez de
910 Castro, J.M., Carbonell, E., 2015. Evaluating the suitability of extended-range
911 luminescence dating techniques over Early and Middle Pleistocene timescales:
912 published datasets and case studies from Atapuerca, Spain. Quaternary
913 International 389, 167-190.
914 Athy, L.F., 1930. Density, porosity and compaction of sedimentary rocks. Bulletin of the
915 American Association of Petroleum Geologists 14, 1-24.
916 Auclair, M., Lamothe, M., Huot, S., 2003. Measurement of anomalous fading for
917 feldspar IRSL using SAR. Radiation Measurements 37, 487-492.

Bailey, R. M., Arnold, L. J., 2006. Statistical modelling of single grain quartz De distributions and an assessment of procedures for estimating burial dose. Quaternary Science Reviews 25, 2475–2502.

Bakker, P., Renssen, H., 2014. Last Interglacial model-data mismatch of thermal maximum temperatures partially explained. Climate of the Past 10, 1633-1644.

Balch, D., Cohen, A., Schnurrenberger, D., Haskell, B., Valero-Garces B., Beck, W., Cheng H., Edwards, L. 2005. Ecosystem and paleohydrological response to Quaternary climate change in the Bonneville Basin, Utah. Palaeogeography, Palaeoclimatology, Palaeoecology 221, 99– 122.

Barry, R.G., Chorley, R.J., 1992. Atmosphere, Weather and Climate. Routledge, London.

Bischoff JL, Cummins K., 2001. Wisconsin Glaciation of the Sierra Nevada (79,000–15,000 yr B.P.) as Recorded by Rock Flour in Sediments of Owens Lake, California. Quaternary Research 55, 14–24.

Blaauw, M., Christen, J.A., 2011. Flexible paleoclimate age-depth models using an autoregressive gamma process. Bayesian Analysis 6, 457–474. Blockley, S.P.E., Pyne-O'Donnell, S.D.F., Lowe, J.J., Matthews, I.P., Stone, A., Pollard, A.M., Turney, C.S.M., Molyneux, E.G., 2005. A new and less destructive laboratory procedure for the physical separation of distal glass tephra shards from sediments. Quaternary Science Reviews 24, 1952–1960.

Blockley, S.P.E., Lane, C.S., Lotter, A.F., Pollard, A.M., 2007. Evidence for the presence of the Vedde Ash in Central Europe. Quaternary Science Reviews 26, 25-28, 3030-3036.

940 Blockley, S.P.E., Ramsey, C.B., Pyle, D.M., 2008. Improved age modelling and high-
941 precision age estimates of late Quaternary tephras, for accurate palaeoclimate
942 reconstruction. Journal of Volcanology and Geothermal Research 177, 251-262.
943 Bowler, J.M., Johnston, H., Olley, J.M., Prescott, J.R., Roberts, R.G., Shawcross, W.,
944 Spooner, N.A., 2003. New ages for human occupation and climatic change at
945 Lake Mungo, Australia. Nature 421, 837-840.
946 Bischoff, J.L., Cummins, K., 2001. Wisconsin Glaciation of the Sierra Nevada (79,000–
947 15,000 yr B.P.) as Recorded by Rock Flour in Sediments of Owens Lake, California.
948 Quaternary Research 55, 14–24.
949 Bolós, X., Martí, J., Becerril, L., Planagumà, LL., Grosse, P., Barde-Cabusson, S., 2015.
950 Volcano-structural analysis of La Garrotxa Volcanic Field (NE Iberia): Implications
951 for the plumbing system. Tectonophysics 642, 58-70.
952 Brauer, A., Allen, J.R.M., Mingram, J., Dulski, P., Wulf, S., Huntley, B., 2007a. Evidence
953 for last interglacial chronology and environmental change from Southern Europe.
954 PNAS 104, 450-455.
955 Brennan, B.J., 2003. Beta doses to spherical grains. Radiation Measurements 37, 299-
956 303.
957 Broecker, W.S., 2000. Abrupt climate change: causal constraints provided by the
958 paleoclimate record. Earth-Science Reviews 51, 137-154.Brown, E.T., Werne, J.P.,
959 Lozano-García, S., Caballero, M., Ortega-Guerrero, B., Cabral-Cano, E., Valero-
960 Garces, B.L., Schwalb, A. and Arciniega-Ceballos, A., 2012. Scientific drilling in the
961 basin of Mexico to evaluate climate history, hydrological resources, and seismic
962 and volcanic hazards. Scientific Drilling 14, 72-75.

963 Carrión, J.S., Leroy, S., 2010. Iberian floras through time: land of diversity and survival.
964 Review of Palaeobotany and Palynology 162, 227-230.
965 Chadima, M. and Hrouda, F., 2009. Remasoft 3.0 Paleomagnetic Data Browser and
966 Analyzer. Agico. Inc., Czech Republic.
967 Channell, J.E.T., 2006. Late brunhes polarity excursions (mono lake, laschamp, iceland
968 basin and pringle falls) recorded at odp site 919 (Irminger basin). Earth and
969 Planetary Science Letters 244, 378-393.
970 Cheng, H., Edwards, L.R., Hoff, J., Gallup, C.D., Richards, D.A., Asmerom, Y., 2000. The
971 half-lives of uranium-234 and thorium-230. Chemical Geology 169, 17–33.
972 Cheng, H., Lawrence Edwards, R., Shen, C.-C., Polyak, V.J., Asmerom, Y., Woodhead, J.,
973 Hellstrom, J., Wang, Y., Kong, X., Spötl, C., Wang, X., Calvin Alexander, E., 2013.
974 Improvements in 230Th dating, 230Th and 234U half-life values, and U–Th
975 isotopic measurements by multi-collector inductively coupled plasma mass
976 spectrometry. Earth and Planetary Science Letters 371–372, 82–91.
977 Clarke, M.L., Rendell, H.M., 1997. Infra-red stimulated luminescence spectra of alkali
978 feldspars. Radiation Measurements 27, 221 – 236.Cohen, A. 2003.
979 Paleolimnology. The History and Evolution of Lake Systems. Oxford University
980 Press. 528 p.
981 Dahl-Jensen, D., Albert, M.R., Aldahan, A., Azuma, N., Balslev-Clausen, D.,
982 Baumgartner, M., Berggren, A.M., Bigler, M., Binder, T., Blunier, T. and
983 Bourgeois, J.C., 2013. Eemian interglacial reconstructed from a Greenland folded
984 ice core. Nature, 493, 489-494.Davies, S.M., Larsen, G., Wastegård, S., Turney,
985 C.S.M., Hall, V.A., Coyle, L., Thordarson, T., 2010. Widespread dispersal of

Icelandic tephra: how does the Eyjafjöll eruption of 2010 compare to past
Icelandic events? Journal of Quaternary Science 25, 605–611.
de Beaulieu, J.-L., Reille, M., 1989. The transition from temperate phases to stadials in
the long Upper Pleistocene sequence from Les Echets (France). Palaeogeography,
Palaeoclimatology, Palaeoecology 72, 147-159.
Demuro, M., Roberts, R. G., Froese, D. G., Arnold, L. J., Brock, F., Bronk Ramsey, C.,
2008. Optically stimulated luminescence dating of single and multiple grains of
quartz from perennially frozen loess in western Yukon Territory, Canada:
comparison with radiocarbon chronologies for the late Pleistocene Dawson
tephra. Quaternary Geochronology 3, 346–364.
Demuro, M., Arnold, L.J., Froese, D.G., Roberts, R.G., 2013. OSL dating of loess deposits
bracketing Sheep Creek tephra beds, northwest Canada: dim and problematic
single-grain OSL characteristics and their effect on multi-grain age estimates.
Quaternary Geochronology 15, 67-87.
Di Rita, F., Fletcher,W.J., Aranbarri, J., Margaritelli, G., Lirer, F., Magri, D., 2018.
Holocene forest dynamics in central and western Mediterranean: periodicity,
spatio-temporal patterns and climate influence. Scientific Reports 8, 8929.
Duller, G.A.T., 2007. Assessing the error on equivalent dose estimates derived from
single aliquot regenerative dose measurements. Ancient TL 25, 15-24.
Edwards, R.L, Chen, J.H, Wasserburg, G.J., 1987. 238U-234U-230Th-232Th systematics
and the precise measurements of time over the past 500.000 years. Earth and
Planetary Science Letters 81, 175–192.
Fritz, S.C., Baker, P.A., Seltzer, G.O., Ballantyne, A., Tapia, P., Cheng, H., Edwards, R.L.,
2007. Quaternary glaciation and hydrologic variation in the South American

1010 tropics as reconstructed from the Lake Titicaca drilling project. Quaternary
1011 Research 68, 410-420.
1012 Galbraith, R.F., Roberts, R.G., Laslett, G.M., Yoshida, H., Olley, J.M., 1999. Optical
1013 dating of single and multiple grains of quartz from Jinmium rock shelter,
1014 northern Australia: Part I, experimental design and statistical models.
1015 Archaeometry 41, 339-364.
1016 Gallagher, K., Lambeck, K. 1989. Subsidence, sedimentation and sea-level changes in
1017 the Eromanga Basin, Australia. Basin Research 2, 115-131.
1018 García-Prieto, E., 2015. Dinámica paleoambiental durante los últimos 135.000 años en
1019 el Alto Jiloca: el registro lacustre de El Cañizar (PhD Thesis). Universidad de
1020 Zaragoza, Spain.
1021 García-Ruiz, J. M., Valero-Garcés, B. L., Martí-Bono, C., González-Sampériz, P., 2003.
1022 Asynchroneity of maximum glacier advances in the central Spanish Pyrenees.
1023 Journal of Quaternary Science 18, 61-72.
1024 García-Ruiz, J.M., López-Moreno, J.I., Vicente-Serrano, S., Lasanta-Martínez, T.,
1025 Beguería, S., 2011. Mediterranean water resources in a global change scenario.
1026 Earth-Science Reviews 105, 121-139.
1027 Giorgi, F., Lionello, P., 2008. Climate change projections for the Mediterranean region.
1028 Global and Planetary Change 63, 90-104.
1029 González-Sampériz, P., Valero-Garcés, B.L., Moreno, A., Morellón, M., Navas, A.,
1030 Machín, J., Delgado-Huertas, A. 2008. Vegetation changes and hydrological
1031 fluctuations in the Central Ebro Basin (NE Spain) since the Late Glacial period:
1032 saline lake records. Palaeogeography, Palaeoclimatology, Palaeoecology 259,
1033 157-181.

González-Sampériz, P., Leroy, S.A.G., Carrión, J.S., Fernández, S., García-Antón, M., Gil-García, M.J., Uzquiano, P., Valero-Garcés, B., Figueiral, I., 2010. Steppes, savannahs, forests and phytodiversity reservoirs during the Pleistocene in the Iberian Peninsula. Review of Palaeobotany and Palynology 162, 427-457.

González-Sampériz, P., García-Prieto, E., Aranbarri, J., Valero-Garcés, B.L., Moreno, A., Gil-Romera, G., Sevilla-Callejo, M., Santos, L., Morellón, M., Mata, P., Andrade, A., Carrión, J.S., 2013. Reconstrucción paleoambiental del último ciclo glacial en la Iberia continental: la secuencia del Cañizar de Villarquemado (Teruel). Cuadernos de Investigación Geográfica 39, 49–76.

González-Sampériz, P., Aranbarri, J., Pérez-Sanz, A., Gil-Romera, G., Moreno, A., Leunda, M., Sevilla-Callejo, M., Corella, J.P., Morellón, M., Oliva, B., Valero-Garcés, B., 2017. Environmental and Climate Change in the Southern Central Pyrenees since the Last Glacial Maximum: a View from the Lake Records. Catena 149, 668-688.

Goring, S.J., Williams, J.W., Blois, J.L., Jackson, S.T., Paciorek, C.J., Booth, R.K., Marlon, J.R., Blaauw, M., Christen, J.A., 2012. Deposition times in the northeastern United States during the Holocene: establishing valid priors for Bayesian age models. Quaternary Science Reviews 48, 54-60.Gracia, F.J., Gutiérrez, F., Gutiérrez, M., 2003. The Jiloca karst polje-tectonic graben (Iberian Range, NE Spain). Geomorphology 52, 215–231.

Guérin, G., Mercier, N., Adamiec, G., 2011. Dose-rate conversion factors: update. Ancient TL 29, 5-8.

Guiot, J., Pons, A., deBeaulieu, J.L., Reille, M., 1989. A 140,000-year continental climate reconstruction from two European pollen records. Nature 338, 309–313.

1058 Gutiérrez-Elorza, M., Gracia, F.J., 1997. Environmental interpretation and
1059 evolution of the Tertiary erosion surfaces in the Iberian Range (Spain). Geological
1060 Society, London, Special Publications 120, 147–158.
1061 Gutiérrez, F., Gutiérrez-Elorza, M., Gracia, F.J., McCalpin, J.P., Lucha, P., Guerrero, J.,
1062 2008. Plio-Quaternary extensional seismotectonics and dreinage natural
1063 development in the central sector of the Iberian Chain (NE Spain).
1064 Geomorphology 102, 21-42.
1065 Gutiérrez, F., Gracia, F.J., Gutiérrez, M., Lucha, P., Guerrero, J., Carbonel, D., Galve, J.P.,
1066 2012. A review on Quaternary tectonic and nontectonic faults in the central
1067 sector of the Iberian Chain, NE Spain. Journal of Iberian Geology 38 (1), 145–160.
1068 Haywood, C., 2012. High spatial resolution electron probe microanalysis of tephras and
1069 melt inclusions without beam-induced chemical modification. The Holocene 22
1070 (1), 119–125.
1071 Heegaard, E., Birks, H.J.B., Telford, R.J., 2005. Relationships between calibrated ages
1072 and depth in stratigraphical sequences: an estimation procedure by mixed effect
1073 regression. The Holocene 15, 1-7.
1074 Helmens, K.F., 2014. The last interglacial-glacial cycle (MIS 5-2) re-examined based on
1075 long proxy records from central and northern Europe. Quaternary Science
1076 Reviews 86, 115-123.
1077 Höbig, N., Weber, M.E., Kehl, M., Weniger, G.-H., Julià, R., Melles, M., Fülöp, R.-H.,
1078 Vogel, H., Reicherter, K., 2012. Lake Banyoles (northeastern Spain): A Last Glacial
1079 to Holocene multi-proxy study with regard to environmental variability and
1080 human occupation. Quaternary International 274, 205-218.

1081 Hodell, D.A., Anselmetti, F.S., Ariztegui, D., Brenner, M., Curtis, J.H., Gilli, A., Grzesik,
1082 D.A., Guilderson, T.J., Mnller, A.D., Bush, M.B., Correa-Metrio, A., Escobar, J.,
1083 Kutterolf, S., 2008. An 85-ka record of climate change in lowland Central
1084 America. Quaternary Science Reviews 27, 1152-1165. Hoek, W.Z., Yu, Z.C., Lowe,
1085 J.J., 2008. INTegration of Ice-core, MArine, and TErrestrial records (INTIMATE):
1086 refining the record of the Last Glacial-Interglacial Transition. Quaternary Science
1087 Reviews 27, 1-5.
1088 Hogg, A., Palmer, J., Boswijk, G., Turney, C., 2011. High-precision radiocarbon
1089 measurements of tree-ring dated wood from New Zealand: 195 BC-AD 995.
1090 Radiocarbon 53 (3), 529-542.
1091 Huntley, D. J., Lamothe, M., 2001. Ubiquity of anomalous fading in K-feldspars and the
1092 measurement and correction for it in optical dating. Canadian Journal of Earth
1093 Sciences 38, 1093-1106.
1094 Jalut, G., Dedoubat, J.J., Fontugne, M., Otto, T., 2009. Holocene circum-Mediterranean
1095 vegetation changes: climate forcing and human impact. Quaternary International
1096 200, 4-18.
1097 Johnson, E.A., Murphy, T., Torreson, O.W., 1948. Pre-history of the Earth's magnetic
1098 field. Journal of Geophysical Research 53(4), 349-372.
1099 Kadereit, A., DeWitt, R., Johnson, T.C., 2012. Luminescence properties and optically
1100 (post-IR blue-light) stimulated luminescence dating of limnic sediments from
1101 northern Lake Malawi – Chances and limitations. Quaternary Geochronology 10,
1102 160-166.

1103 Kirschvink, J.L., 1980. The least-squares line and plane and the analysis of
1104 paleomagnetic data. Geophysical Journal of the Royal Astronomical Society 62,
1105 669-718.
1106 Kuehn, S.C.,Froese, D.G., 2010. Tephra from Ice-A Simple Method to Routinely Mount,
1107 Polish, and Quantitatively Analyze Sparse Fine Particles. Microscopy and
1108 Microanalysis 16 (2), 218–225.
1109 Kuehn, S.C., Froese, D.G., Shane, P.A.R., INTAV Intercomparison Participants., 2011.
1110 The INTAV intercomparison of electron-beam microanalysis of glass by
1111 tephrochronology laboratorios: Results and recommendations. Quaternary
1112 International 246 (1–2), 19–47.
1113 Kukla, G., McManus, J.F., Rousseau, D.-D., Chuine, I., 1997. How long and stable was
1114 the Last Interglacial. Quaternary Science Reviews 16, 605–612.
1115 Lane, C.S., Lowe, D.J., Blockley, S.P.E., Suzuki, T. and Smith, V.C., 2017. Advancing
1116 tephrochronology as a global dating tool: Applications in volcanology, archaeology, and
1117 palaeoclimatic research. Quaternary Geochronology 40, 1-7.
1118 Lézine, A.M., von Grafenstein, U., Andersen, N., Belmecheri, S., Bordon, A., Caron, B.,
1119 Cazet, J.P., Erlenkeuser, H., Fouache, E., Grenier, C., Huntsman-Mapila, P.,
1120 Hureau-Mazaudier, D., Manelli, D., Mazaud, A., Robert, C., Sulpizio, R., Tiercelin,
1121 J.J., Zanchetta, G., Zeqollari, Z., 2010. Lake Ohrid, Albania, provides an
1122 exceptional multi-proxy record of environmental changes during thelast glacial–
1123 interglacial cycle. Palaeogeography, Palaeoclimatology, Palaeoecology 287, 116–
1124 127.
1125 Lewis, C., McDonald, E., Sancho, C., Peña, J.L., Rhodes, E., 2009. Climatic implications of
1126 correlated Upper Pleistocene glacial and fluvial deposits on the Cinca and Gállego

1127 Rivers (NE Spain) based on OSL dating and soil stratigraphy. Global and Planetary
1128 Change 67, 141-152.
1129 Lisiecki, L. E., Raymo, M. E. 2005. A Pliocene-Pleistocene stack of 57 globally
1130 distributed benthic d18O records. Paleoceanography 20, PA2007.
1131 Litt, T., Krastel, S., Sturm, M., Kipfer, R., Örcen, S., Heumann, G., Franz, S.O., Ülgen,
1132 U.B., Niessen, F., 2009. "PALEOVAN", International Continental Scientific Drilling
1133 Program (ICDP): site survey results and perspectives. Quaternary Science
1134 Reviews 28, 1555-1567.
1135 Lionello, P, Mallanotte-Rizzoli, P, and Boscolo, R. (ed). 2012. Mediterranean Climate
1136 Variability. Developments in Earth and Environmental Sciences, Elsevier, 421 p.
1137 Lopez-Martín, F., Cabera, M., Cuadrat, J.M., 2007. Atlas Climático de Aragón.
1138 Departamento de Medio Ambiente, Gobierno de Aragón, Zaragoza.Lukas, S.,
1139 Preusser, F., Anselmetti, F.S., Tinner, W., 2012. Testing the potential of
1140 luminescence dating of high-alpine lake sediments. Quaternary Geochronology 8,
1141 23-32.
1142 Lukas, S., Preusser, F., Anselmetti, F.S., Tinner, W., 2012. Testing the potential of
1143 luminescence dating of high-alpine lake sediments. Quaternary Geochronology 8,
1144 23-32.
1145 Lunt, D.J., Abe-Ouchi, A., Bakker, P., Berger, A., Braconnot, P., Charbit, S., Fischer, N.,
1146 Herold, N., Jungclaus, J.H., Khon, V.C., Krebs-Kanzow, U., Langebroek, P.M.,
1147 Lohmann, G., Nisancioglu, K.H., Otto-Bliesner, B.L., Park, W., Pfeiffer, M., Phipps,
1148 S.J., Prange, M., Rachmayani, R., Renssen, H., Rosenbloom, N., Schneider, B.,
1149 Stone, E.J., Takahashi, K., Wei, W., Yin, Q., Zhang, Z.S., 2013. A multi-model
1150 assessment of Last Interglacial temperatures. Climate of the Past 9, 699-

1151 717.Magri, D., Tzedakis, P.C., 2000. Orbital signatures and long-term vegetation
1152 patterns in the Mediterranean. Quaternary International 73-74, 69–78.
1153 Magri, D., Di Rita, F., Aranbarri, J., Fletcher, W., González-Sampériz, P., 2017.
1154 Quaternary disappearance of tree taxa from Southern Europe: timing and trends.
1155 Quaternary Science Reviews 163, 23-55.
1156 Martrat, B., Grimalt, J.O., Lopez-Martinez, C., Cacho, I., Sierro, F.J., Flores, J.A., Zahn, R.,
1157 Canals, M., Curtis, J.A., Hodell, D.A., 2004. Abrupt temperature changes in the
1158 western Mediterranean over the past 250,000 years. Science 306, 1762-1765.
1159 Mejdahl, V., 1979. Thermoluminescence dating: beta-dose attenuation in quartz
1160 grains. Archaeometry 21, 61-72.
1161 Mejdahl, V., 1987. Internal radioactivity in quartz and feldspar grains. Ancient TL 5, 10-
1162 17.
1163 Melles, M., Brigham-Grette, J., Minyuk, P.S., Nowaczyk, N.R., Wennrich, V., DeConto,
1164 R.M., Anderson, P.M., Andreev, A.A., Coletti, A., Cook, T.L., HaltiaHovi, E.,
1165 Kukkonen, M., Lozhkin, A.V., Rosen, P., Tarasov, P., Vogel, H., Wagner, B., 2012.
1166 2.8 million years of arctic climate change from Lake El'gygytgyn, NE Russia.
1167 Science 337 (6092), 315-320.
1168 Moore, R.B., 1990. Volcanic geology and eruption frequency, São Miguel, Azores.
1169 Bulletin of Volcanology 52, 602–614.
1170 Morellón, M., Aranbarri, J., Moreno, A., González-Sampériz, P., Valero-Garcés, B. L.,
1171 2018. Early Holocene humidity patterns in the Iberian Peninsula reconstructed
1172 from lake, pollen and speleothem records. Quaternary Science Reviews 181, 1-
1173 18.

1174 Moreno, A., Cacho, I., Canals, M., Grimalt, J.O., Sanchez-Goni, F., Shackleton, N., Sierro,
1175 F.J., 2005. Links between marine and atmospheric processes oscillating on a
1176 millennial time-scale. A multi-proxy study of the last 50,000 yr from the Alboran
1177 Sea (Western Mediterranean Sea). Quaternary Science Reviews 24, 1623-1636.
1178 Moreno, A., González-Sampériz, P., Morellón, M., Valero-Garcés, B.L., Fletcher, W.J.,
1179 2012. Northern Iberian abrupt climate change dynamics during the last glacial
1180 cycle: A view from lacustrine sediments. Quaternary Science Reviews 36, 139-
1181 153.
1182 Murray, A.S., Wintle A.G., 2000. Luminescence dating of quartz using an improved
1183 single-aliquot regenerative-dose procedure. Radiation Measurements 32, 57-73.
1184 Murray, A.S., Wintle, A.G., 2003. The single-aliquot regenerative dose protocol:
1185 potential for improvements and reliability. Radiation Measurements 37, 377-381.
1186 Murray, A.S., Roberts, R.G., 1997. Determining the burial time of single grains of quartz
1187 using optically stimulated luminescence. Earth and Planetary Science Letters 152,
1188 163–180.
1189 Nambi, K.S.V., Aitken, M.J., 1986. Annual dose conversion factors for TL and ESR
1190 dating. Archaeometry 28, 202-205.
1191 Olley, J.M., Caitcheon, G.G., Roberts, R.G., 1999. The origin of dose distribution in
1192 fluvial sediments, and the prospect of dating single grains from fluvial deposits
1193 using optically stimulated luminescence. Radiation Measurements 30, 207–217.
1194 Olley, J.M., Pietsch, T., Roberts, R.G., 2004a. Optical dating of Holocene sediments
1195 from a variety of geomorphic settings using single grains of quartz.
1196 Geomorphology 60, 337–358.

1197 Olley, J.M., De Deckker, P., Roberts, R.G., Fifieldd, L.K., Yoshida, H., Hancock, G., 2004b.
1198 Optical dating of deep-sea sediments using single grains of quartz: a comparison
1199 with radiocarbon. Sedimentary Geology 169, 175-189.
1200 Ojala, A.E.K., Francus, P., Zolitschka, B., Besonen, M., Lamoureux, S.F., 2012.
1201 Characteristics of sedimentary varve chronologies e a review. Quaternary Science
1202 Reviews 43, 45-60.
1203 Ogg, J.G., Ogg, G., Gradstein, F.M., 2016. A Concise Geologic Time Scale: 2016. Elsevier,
1204 234 p.
1205 Opdyke, N. D, Channel, J.E.T., 1996. Magnetic stratigraphy. International Geophysics
1206 Series. Academic Press 64, 346 p.
1207 Osete, M.L., Martín-Chivelet, J., Rossi, C., Edwards, R.L., Egli, R., Muñoz-García, M.B.,
1208 Wang, X., Pavón-Carrasco, F.J., Heller, F., 2012. The Blake geomagnetic excursion
1209 recorded in a radiometrically dated speleothem. Earth and Planetary Science
1210 Letters 353, 173-181.
1211 Otto-Bliesner, B., Rosenbloom, N., Stone, E., McKay, N.P., Lunt, D.J., Brady, E.C.,
1212 Overpeck, J.T., 2013. How warm was the Last Interglacial? New model-data
1213 comparisons. Philosophical transactions. Series A, Mathematical, physical, and
1214 engineering sciences 371, 20130097.Pérez-Mejías, C., Moreno, A., Sancho, C.,
1215 Bartolomé, M., Stoll, H., Cacho, I., Cheng, H., Edwards, R.L., 2017. Abrupt climate
1216 changes during Termination III in Southern Europe. Proceedings of the National
1217 Academy of Sciences of the United States of America 114, 10047–10052.
1218 Placzek C, Patchett PJ, Quade J, Wagner, J.D.M., 2006a. Strategies for successful U-Th
1219 dating of paleolake carbonates: An example from the Bolivian Altiplano.
1220 Geochemistry, Geophysics, Geosystems 7, Q05024.

1221 Placzek, C., Quade, J., Patchett, P.J., 2006b. Geochronology and stratigraphy of late
1222 Pleistocene lake cycles on the southern Bolivian Altiplano: implications for causes
1223 of tropical climate change. Geological Society of America Bulletin 118, 515–532.
1224 Prescott, J.R., Hutton, J.T., 1994. Cosmic ray contribution to dose rates for
1225 luminescence and ESR dating: Large depths and long-term time variations.
1226 Radiation Measurements 23, 497-500.
1227 Preusser, F., 2003. IRSL dating of K-rich feldspars using the SAR protocol: comparison
1228 with independent age control. Ancient TL 21, 17–23.Ramsey, C.B., 2009.
1229 Bayesian analysis of radiocarbon dates. Radiocarbon 51 (1), 337-360.Rasmussen,
1230 S.O., Bigler, M., Blockley, S.P., Blunier, T., Buchardt, S.L., Clausen, H.B., Cvijanovic,
1231 I., Dahl-Jensen, D., Johnsen, S.J., Fischer, H., Gkinis, V., Guillevic, M., Hoek, W.Z.,
1232 Lowe, J.J., Pedro, J.B., Popp, T., Seierstadt, I.K., Steffensen, J.P., Svensson, A.M.,
1233 Vallelonga, P., Vinther, B.M., Walker, M.J.C., Wheatley, J.J., Winstrup, M., 2014. A
1234 stratigraphic framework for abrupt climate changes during the Last Glacial period
1235 based on three synchronized Greenland ice-core records: refining and extending
1236 the INTIMATE event stratigraphy. Quaternary Science Reviews 106, 14-28.
1237 Rees-Jones, J., 1995. Optical dating of young sediments using fine-grain quartz. Ancient
1238 TL 13, 9-14.
1239 Reille, M., de Beaulieu, J.-L., Svobodova, H., Andrieu-Ponel, V., Goeury, C., 2000. Pollen
1240 analytical biostratigraphy of the last five climatic cycles from a long continental
1241 sequence from the Velay region (Massif Central, France). Journal of Quaternary
1242 Science 15, 665-685.
1243 Reimer, P.J., Baillie, M.G.L., Bard, E., Bayliss, A., Beck, J.W., Bertrand, C.J.H., Blackwell,
1244 P.G., Buck, C.E., Burr, G.S., Cutler, K.B., Damon, P.E., Edwards, R.L., Fairbanks,

1245 R.G., Friedrich, M., Guilderson, T.P., Hogg, A.G., Hughen, K.A., Kromer, B.,
1246 McCormac, G., Manning, S., Bronk Ramsey, C., Reimer, R.W., Remmele, S.,
1247 Southon, J.R., Stuiver, M., Talamo, S., Taylor, F.W., van der Plicht, J.,
1248 Weyhenmeyer, C.E., 2004. IntCal04 terrestrial radiocarbon age calibration, 0-26
1249 cal kyr . Radiocarbon 46 (3), 1029-1058.
1250 Reimer, P.J., Baillie, M.G.L., Bard, E., Bayliss, A., Beck, J.W., Blackwell, P.G., Bronk
1251 Ramsey, C., Buck, C.E., Burr, G.S., Edwards, R.L., Friedrich, M., Grootes, P.M.,
1252 Guilderson, T.P., Hajdas, I., Heaton, T.J., Hogg, A.G., Hughen, K.A., Kaiser, K.F.,
1253 Kromer, B., McCormac, F.G., Manning, S.W., Reimer, R.W., Richards, D.A.,
1254 Southon, J.R., Talamo, S., Turney, C.S.M., van der Plicht, J., Weyhenmeyer, C.E.,
1255 2009. IntCal09 and Marine09 radiocarbon age calibration curves, 0-50,000 years
1256 cal . Radiocarbon 51, 1111-1150
1257 Reimer, P.J., Bard, E., Bayliss, A., Beck, J.W., Blackwell, P.G., Bronk Ramsey, C., Buck,
1258 C.E., Cheng, H., Edwards, R.L., Friedrich, M., Grootes, P.M., Guilderson, T.P.,
1259 Haflidason, H., Hajdas, I., Hatte, C., Heaton, T.J., Hoffmann, D.L., Hogg, A.G.,
1260 Hughen, K.A., Kaiser, K.F., Kromer, B., Manning, S.W., Niu, M., Reimer, R.W.,
1261 Richards, D.A., Scott, E.M., Southon, J.R., Staff, R.A., Turney, C.S.M., van der
1262 Plicht, J., 2013. IntCal 13 and Marine 13 radiocarbon age calibration curves 0-
1263 50,000 years cal . Radiocarbon 55, 1869-1887.
1264 Rendell, H.M., 1985. The precision of water content estimates in the
1265 thermoluminescence dating of loess from northern Pakistan. Nuclear Tracks and
1266 Radiation Measurements 10, 763-768.
1267 RESET (RESponse of humans to abrupt Environmental Transitions). Website:
1268 http://c14.arch.ox.ac.uk/reset/embed.php?File=index.html

1269 Revuelta, M.A., Sastre, M., Fernández, A.J., Martin, L., Gómez-Moreno, F.J., Artinano,
1270 B., Pujadas, M., Molero, F., 2012. Characterization of the Eyjafjallajökull volcanic
1271 plume over the Iberian Peninsula by lidar remote sensing and ground-level data
1272 collection. Atmospheric Environment 48, 46–55.
1273 Roberts, A.P., 2015. Magnetic mineral diagenesis. Earth-science reviews, 151, 1-47.
1274 Rodbell, D.T., Abbott, M.B., 2012. Workshop on Drilling of Lake Junin, Peru: Potential
1275 for Development of a Continuous Tropical Climate Record. Scientific Drilling 13,
1276 58-60.
1277 Rubio, J.C., 2004. Contexto hidrogeológico e histórico de los humedales del Cañizar.
1278 Consejo de la Protección de la Naturaleza de Aragón, Serie de Investigración,
1279 Zaragoza.
1280 Rubio, J.C, Simon, J.L., 2007, Tectonic subsidence v, erosional lowering in a
1281 controversial intramontane depression: the Jiloca basin (Iberian Chain, Spain),
1282 Geological Magazine 144, 127-141.
1283 Russell, J.M., Bijaksana, S., Vogel, H., Melles, M., Kallmeyer, J., Ariztegui, D., Crowe, S.,
1284 Fajar, S., Hafidz, A., Haffner, D., Hasberg, A., Ivory, S., Kelly, C., King, J., Kirana, K.,
1285 Morlock, M., Noren, A., O'Grady, R., Ordonez, L., Stevenson, J., von Rintelen, T.,
1286 Vuillemin, A., Watkinson, I., Wattrus, N., Wicaksono, S., Wonik, T., Bauer, K.,
1287 Deino, A., Friese, A., Henny, C., Imran, Marwoto, R., Ngkoimani, L.O.,
1288 Nomosatryo, S., Safiuddin, L.O., Simister, R., Tamuntuan, G., 2016. The Towuti
1289 Drilling Project: paleoenvironments, biological evolution, and geomicrobiology of
1290 a tropical Pacific lake. Scientific Drilling 21, 29-40.

1291 Sánchez-Goñi, M.F., Eynaud, F., Turon, J.L., Shackleton, N.J., 1999. High resolution
1292 palynological record off the Iberian margin: direct land–sea correlation for the
1293 last interglacial complex. Earth and Planetary Science Letters 171, 123-137.
1294 Sánchez-Goñi, M.F., Turon, J.L., Eynaud, F., Gendreau, S., 2000. European climatic
1295 response to millenial-scale changes in the atmosphere-ocean system during the
1296 Last Glacial period. Quaternary Research 54, 394–403.
1297 Sánchez-Goñi, M.F., Loutre, M.F., Crucifix, M., Peyron, O., Santos, L., Duprat, J.,
1298 Malaizé, B., Turon, J.L., Peypouquet, J.P., 2005. Increasing vegetation and climate
1299 gradient in Western Europe over the Last Glacial Inception (122–110 ka): data-
1300 model comparison. Earth and Planetary Science Letters 231 (1–2), 111–130.
1301 Sancho, C., Arenas, C., Pardo, G., Peña-Monné, J. L., Rhodes, E. J., Bartolomé, M.,
1302 García-Ruiz, J.M., Martí-Bono, C., 2018. Glaciolacustrine deposits formed in an
1303 ice-dammed tributary valley in the south-central Pyrenees: new evidence for late
1304 Pleistocene climate. Sedimentary Geology 366, 47-66.
1305 Schnurrenberger, D., Russell, J., Kelts, K., 2003. Classification of lacustrine sediments
1306 based on sedimentary components. Journal of Paleolimnology 29, 141–154.
1307 Shackleton, N.J., Chapman, M., Sánchez-Goñi, M.F., Pailler, D., Lancelot, Y., 2002. The
1308 classic marine isotope substage 5e. Quaternary Research 58, 14–16.Sheldon,
1309 N.D., Retallack, G.J., 2001. Equation for compaction of paleosols due to burial.
1310 Geology 29, 247-250.
1311 Shen, C.-C., Edwards, R.L., Cheng, H., Dorale, J.A., Thomas, R.B., Moran, S.B.,
1312 Weinstein, S.E., Edmonds, H.N., 2002. Uranium and thorium isotopic
1313 concentration measurements by magnetic sector inductively coupled plasma
1314 mass spectrometry. Chemical Geology 185, 165–178. Sier, M.J., Peeters, J.,

1315 Dekkers, M.J., Pares, J.M., Chang, L., Busschers, F.S.B., Cohen, K.M., Wallinga, J.,
1316 Bunnik, F.P., Roebroeks, W., 2015. The Blake Event recorded near the Eemian
1317 Type locality e a diachronic onset of the Eemian in Europe. Quaternary
1318 Geochronology 28, 12-28. Stein, M., Ben-Avraham, Z., Goldstein, S., Agnon, A.,
1319 Ariztegui, D., Brauer, A., Haug, G., Ito, E., Yasuda, Y., 2011. Deep drilling at the
1320 Dead Sea. Scientific Drilling 46-47.
1321 Stevenson, J.A., Loughlin, S., Rae, C., Thordarson, T., Milodowski, A.E., Gilbert, J.S.,
1322 Harangi, S., Lukács, R., Højgaard, B., Árting, U., Pyne-O'Donnell, S., MacLeod, A.,
1323 Whitney, B., Cassidy, M., 2012. Distal deposition of tephra from the
1324 Eyjafjallajökull 2010 summit eruption. Journal of Geophysical Research 117,
1325 B00C10.
1326 Stevenson, J.A., Millington, S.C., Beckett, F.M., Swindles, G.T., Thordarson, T., 2015. Big
1327 grains go far: understanding the discrepancy between tephrochronology and
1328 satellite infrared measurements of volcanic ash. Atmospheric Measurement
1329 Techniques 8, 2069-2091. Thorarinsson, S., 1967. The eruptions of Hekla in
1330 historical times. A tephrochronological study. The eruption of Hekla 1947-48. 1,
1331 1-170.
1332 Turney, C.S.M., 1998. Extraction of rhyolitic component of Vedde microtephra from
1333 minerogenic lake sediments. Journal of Paleolimnology 19 (2), 199–206.
1334 Turney, C.S.M., Harkness, D.D., Lowe, J.J., 1997. The use of microtephra horizons to
1335 correlate Late-glacial lake sediment successions in Scotland. Journal of
1336 Quaternary Science 12 (6), 525–531.
1337 Tzedakis, P.C., Andrieu, V., de Beaulieu, J.-L., Crowhurst, S., Follieri, M., Hooghiemstra,
1338 H., Magri, D., Reille, M., Sadori, L., Shackleton, N.J., Wijmstra, T.A., 1997.

1339 Comparison of terrestrial and marine records of changing climate of the last
1340 500,000 years. Earth and Planetary Science Letters 150, 171–176.
1341 Tzedakis, P.C., Andrieu, V., Birks, H.J.B., de Beaulieu, J.-L., Crowhurst, S., Follieri, M.,
1342 Hooghiemstra, H., Magri, D., Reille, M., Sadori, L., Shackleton, N.J., Wijmstra,
1343 T.A., 2001. Establishing a terrestrial chronological framework as a basis for
1344 biostratigraphical comparisons. Quaternary Science Reviews 20, 1583–1592.
1345 Tzedakis, P.C., Frogley, M.R., Heaton, T.H.E., 2003. Last Interglacial conditions in
1346 southern Europe, evidence from Ioannina, northwest Greece. Global and
1347 Planetary Change 36, 157–170.
1348 Tzedakis, P.C., Hooghiemstra, H., Pälike, H., 2006. The last 1.35 million years at Tenaghi
1349 Philippon, revised chronostratigraphy and long-term vegetation trends.
1350 Quaternary Science Reviews 25, 3416–3430.
1351 Tzedakis, P.C., 2007. Seven ambiguities in the Mediterranean palaeoenvironmental
1352 narrative. Quaternary Science Reviews 26, 2042–2066.
1353 Valero-Garcés, B., Moreno, A., 2011. Iberian lacustrine sediment records: responses to
1354 past and recent global changes in the Mediterranean region. Journal of
1355 Paleolimnology 46, 319–325.
1356 Valero-Garcés, B., Morellón, M., Moreno, A., Corella, P., Martín-Puertas, C., Barreiro,
1357 F., Pérez, A., Giralt, S., Mata-Campo, M.P., 2014. The carbonate factory in karst
1358 lakes: sources, processes and depositional environments in Quaternary Iberian
1359 Lakes. Sedimentary Geology 299, 1–29.
1360 Van Andel, T.H., Tzedakis, P.C., 1996. Paleolithic landscapes of Europe and environs,
1361 150,000-25,000 years ago: an overview. Quaternary Science Reviews 15, 481-
1362 500.

1363 Wang, Y.J., Cheng, H., Edwards, R.L., An, Z.S., Wu, J.Y., Shen, C.C., Dorale, J.A., 2001. A
1364 high-resolution absolute-dated Late Pleistocene monsoon record from Hulu
1365 Cave, China. Science 294, 2345–2348.Woillard, G.M., Mook, W.G., 1982. Carbon-
1366 14 dates at Grande Pile: correlation of land and sea chronologies. Science 215,
1367 159–161.
1368 Zanchetta, G., Sulpizio, R., Roberts, N., Cioni, R., Eastwood, W.J., Siani, G., Caron, B.,
1369 Paterne, M., Santacroce, R., 2011. Tephrostratigraphy, chronology and climatic
1370 events of the Mediterranean basin during the Holocene: An overview. The
1371 Holocene 21 (1), 33 –52.
1372 Zanchetta, G., Regattieri, E., Giaccio, B., Wagner, B., Sulpizio, R., Francke, A., Vogel,
1373 L.H., Sadori, L., Masi, A., Sinopoli, G., Lacey, J.H., Leng, M.L., Leicher, N., 2016.
1374 Aligning MIS5 proxy records from Lake Ohrid (FYROM) with independently dated
1375 Mediterranean archives: implications for core chronology. Biogeosciences 13,
1376 2757-2768.
1377 Zimmerman, D.W., 1972. Relative thermoluminescence effects of alpha- and beta-
1378 irradiation. Radiation Effects 14, 81-92.
1379 Zolitschka, B., F. Anselmetti, D. Ariztegui, H. Corbella, P. Francus, A. Lücke, N.I.
1380 Maidana, C. Ohlendorf, F. Schäbitz, S. Wastegård, 2013. Environment and climate
1381 of the last 51,000 years – new insights from the Potrok Aike maar lake Sediment
1382 Archive Drilling project (PASADO). Quaternary Science Reviews 71, 1-12.
1383
1384 TABLES
1385
1386 Table 1. Facies, facies associations and depositional environments in VIL sequence.
1387

1388 Table 2. Radiocarbon dates for the VIL sequence. Thirteen rejected dates are indicated
1389 by italics.
1390
1391 Table 3. U/Th samples for the VIL sequence (A) and obtained results (B).
1392
1393 Table 4. Dose rate data, multi-grain aliquot additive dose equivalent doses (De) and
1394 polymineral fine-grain IRSL ages for the VIL samples.
1395
1396 Table 5. Dose rate data, single-grain equivalent doses (De) and quartz OSL ages for the
1397 VIL samples.
1398
1399 Table 6. High-resolution gamma spectrometry results and daughter-to-parent isotopic
1400 ratios for VIL single-grain OSL samples.
1401
1402 FIGURE CAPTIONS
1403 Figure 1. A. Location of Cañizar de Villarquemado Basin. B. Map of the watershed and
1404 maximum surface area of the wetland prior to drainage.
1405
1406 Figure 2. Stratigraphy of VIL sequence: sedimentary facies and associations, units,
1407 depositional environments and location of samples for different dating methods.
1408
1409 Figure 3. a) number of samples and value of NRM in A/m. b to e): stepwise AF
1410 demagnetization for selected samples represented in a stereoplot, orthogonal diagram
1411 and decay of normalized NRM. Observe that only sample d is from a black clay, with
1412 unstable paleomagnetic behavior. The other three samples show two stable
1413 paleomagnetic components. 5.f) Stereographic projection of calculated components.
1414 Viscous represent all the components and in pink the average of all together. In the
1415 other stereoplots the characteristic component of all samples is represented and in
1416 red, the data from the same section (number on top of each steroplot) is highlighted.
1417
1418 Figure 4. Representative single-grain De distributions for the VIL OSL samples, shown

1419 as radial plots. a) Ratios of recovered-to-given dose obtained for individual quartz
1420 grains of V127 in the SAR dose-recovery test. The grey shaded region on the radial plot
1421 is centred on the administered dose for each grain (sample average = 300 Gy).
1422 Individual De values that fall within the shaded region are consistent with the
1423 administered dose at 2s. b) Example of a homogeneous De distribution with limited
1424 dose overdispersion, indicative of a sample that has been sufficiently bleached prior to
1425 deposition. Here, the grey band is centred on the weighted mean De values used to
1426 calculate the OSL age, which was estimated using the central age model of Galbraith et
1427 al. (1999). c) Example of a more scattered De distribution that is not well-represented
1428 by the weighted mean burial dose estimate. This sample is cautiously interpreted as
1429 being heterogeneously bleached prior to deposition and its burial dose estimate
1430 (indicated by the grey bands) has been derived using the minimum age model of
1431 Galbraith et al. (1999).
1432
1433 Figure 5. The Bayesian Age model for the VIL sequence with all the dates included (A)
1434 and the final result with the main sedimentation rate changes indicated (B).
1435
1436 Figure 6. Main geochemical and palynological data of VIL sequence plotted in age with
1437 both sedimentological units (on the left) and MIS periods (on the right) indicated.
1438 Chronological limits for MIS periods follow Lisiecki and Raymo (2005) and Rasmussen
1439 et al. (2014) while stadials and interstadials into MIS 5 chronology follow Martrat et al.
1440 (2004). Pollen groups are composed by the following taxa: Mediterranean includes
1441 evergreen Quercus, Viburnum, Buxus, Oleaceae, Pistacia, Rhamnus, Myrtus,
1442 Thymelaeaceae, Arbutus unedo, Cistaceae and Helianthemum. Steppe includes
1443 Ephedra distachya and E. fragilis types and Chenopodiaceae. Local moisture is formed
1444 by aquatics and Pterydophyta: Cyperaceae, Typhaceae, Juncus, Sparganium,
1445 Thalictrum, Lythrum, Stratiotes, Utricularia, Ledum palustre, Ranunculus, Pedicularis,
1446 Myriophyllum, Lemna, Nymphaea, Nuphar, Potamogeton, Isoetes, Alisma, Callitriche,
1447 Asplenium, Monolete, Trilete, Polypodium, Botrychium, Pteris, Equisetum and
1448 Selaginella. Shaded grey bands show intervals with low pollen productivity in MIS 5b,
1449 MIS 3 and MIS 2.

.

TABLES

Table 1. Summary of sedimentary facies and facies associations in the VIL sequence.

FACIES	Description
SAND	
Grey Sand	Dm to cm thick calcite and silicate sand.
Creamy sand	Cm to dm-thick layers mostly composed of calcite clasts and charophyte remains. Yellowish, brown or white color depending on variable organic, carbonate and silicate contents.
Peaty Sand	Cm-thick, brown carbonate and silicate sand with peat fragments.
Lumaquella	Mm to cm thick, gastropod-rich sand with calcite matrix.
COARSE SILT	
Yellowish silt	Calcite silt with calcite coating, charophyte remains and calcite crystals and intermediate silicate content.
Creamy silt	Calcite silt, dominated by carbonate coating and calcite crystals and lower silicate content than yellowish silt. Variable reddish mottling.

Light grey silt	Calcite and silicate silt with frequent rootlets and grey mottling.
Dark grey silt	Silicate and calcite silt with organic matter and plant remains. Faintly banded. They are the coarsest silt facies.
Peaty silt	Cm thick layers of coarse grey silt with large peat fragments. Abundant mottling.
FINE SILT	
Light grey silt	Silicate and calcite fine silts. Mottling appears in discrete horizons associated to coarser levels with rootlets and plant fragment.
Creamy/white silt	Layers of finer calcite silt, white, more homogeneous, no gastropods. Creamy layers are more massive to faintly banded (cm-scale) coarser calcite silt, with gastropods, larger calcite clasts, charophyte and organic fragments and higher silicate content.
Black and grey silt	Faintly banded, medium size silt dominated by calcite grains (pseudo-oolites, coatings, calcite clasts) and organic fragments. Grey layers are massive to black, mottled with higher silicate content.
Red clayey silt	Dm thick, massive layers of reddish silt dominated by calcite but abundant silicate content and presence of hematite and dolomite.
Laminated grey/greenish silt	Cm to dm-thick layers of calcite and silicate silt.
PEAT	
Massive fine peat	Cm to dm thick, black, massive, homogeneous fine peat.
Coarse peat	Black, massive with coarse peat fragments.
FACIES ASSOCIATIONS	
A. CARBONATE	Sequences composed of creamy and white sands, coarse and fine yellowish silts and organic silts. Minor peat facies. Varied mottling. **Depositional environment:** littoral charophyte-dominated, carbonate lake. Other intervals with sequences composed of grey sands and grey silts. **Depositional environment:** littoral carbonate lake with higher clastic input.
B. CLASTIC	Sequences dominated by grey sands, coarse grey silts, fine grey silts and massive, black mottled silts. Alternations of dark and light grey coarse silts, with some fine black mottled silts. In more distal areas, sequences are dominated by finer, laminated silts. **Depositional environment:** Clastic dominated, higher energy littoral (current and wave influenced) and lower energy sublittoral to distal.
C. WETLAND	Sequences include peat facies (fine and coarse), peaty sands and silts, lumaquellas and organic-rich silts. Some lastic intercalations and carbonate sands. **Depositional environment:** wetland with some minor carbonate lake.
D. DISTAL ALLUVIAL FAN/MUD FLAT	The sequences are composed of grey, massive to banded silts with frequent mottling and some minor sand layers. Some intervals are dominated by red clayey silts with minor grey silts. **Depositional environment:** distal alluvial fan associated to mudflat.

92 Table 2. Radiocarbon ages for the VIL sequence. Rejected ages are indicated by italics.

Sample	Composite Depth (cm)	Laboratory code	$\delta^{13}C$ (‰)	Radiocarbon age (years BP)	Calibrated age (cal yrs BP) range 2σ
VIL05-1A, 11 cm	11	Beta-332033	-27.3	430 ± 30	490 ± 39
VIL05-1A, 132 cm	132	Beta-332034		7460 ± 40	
VIL05-1A, 220 cm	220	Poz-16073		11950 ± 70	
VIL05-1B-1T-2, 2-3 cm	62 ± 5	Beta-319544		2020 ± 30	1974 ± 82
VIL05-1B-1T-2 36-38	96 ± 5	Poz-18451	-28 ± 9	3750 ± 40	4084 ± 100
VIL05-1B-1T-3, 6-7	*135*	*Poz-16073*	*-32 ± 6*	*11950 ± 70*	*13807 ± 190*
VIL05-1B-1T-3 39-40	173.5	Poz-18509	-22 ± 8	7460 ± 50	8279 ± 94
VIL05-1B-1T-4 41-42	233 ± 5	Poz-18453	-27 ± 6	9820 ± 50	11248 ± 76
VIL05-1B-1T-5, 55	307 ± 00	Poz-15943		11620 ± 60	13481 ±174
VIL05-1B-1T-6, 15	*325 ± 4*	*Poz-23667*	*-32 ± 7*	*5760 ± 60*	*6543 ± 134*
VIL05-1B-1T-7, 25	*370 ± 4*	*Poz-23669*	*-25 ± 3*	*6290 ± 40*	*7237 ± 80*
VIL05-1B-1T-7 55-56.5	*417*	*Poz-18510*	*-26 ± 4*	*8200 ± 50*	*9157 ± 143*
VIL05-1B-1T-8 32-35	451 ± 5	Poz-18511	-22 ± 4	15390 ± 100	18680 ± 193
VIL05-1B-1T-10, 15	549 ± 5	Poz-15944		18280 ± 110	21844 ± 373
VIL05-1B-1T-12 16-17	*638 ± 2*	*Poz-18454*	*-25 ± 7*	*22900 ± 280*	*27584 ± 790*
VIL05-1B-1T-14, 5	734 ± 8	Poz-15945		21020 ± 140	25060 ± 503
VIL05-1B-1T-16, 5	861	Poz-15946		22780 ± 160	27447 ± 570
VIL05-1B-1T-18 13-14	*989 ± 5*	*Poz-18455*	*-25 ± 4*	*27000 ± 450*	*31501 ± 840*
VIL05-1B-1T-20, 57	1114 ± 8	Poz-23714	-5 ± 9	25520 ± 380	30269 ± 713
VIL05-1B-1T-24, 12	1322 ± 1	Poz-15948		27900 ± 300	32182 ± 755
VIL 05 -1B-1T- 28, 7 cm	1487 ± 7	Poz-17394	-12 ± 6	33300 ± 800	38285 ± 1892
VIL 05-1B-1T-35, 44 cm	1912 ± 3	Poz-17287	-19 ± 4	36800 ± 800	41589 ± 1348
VIL 05-1B-1T-39, 56 cm	*2177 ± 3*	*Poz-17249*	*-29 ± 3*	*22920 ± 360*	*27592 ± 928*

Table 3. U/Th samples for the VIL sequence (A) and obtained results (B).

A)

Sample ID	Sample weight (g)	Sample name	Composite Depth (m)	Sample type
VIL-1	0.0491	VIL05-1B-1T-61, 40-60	28.9	Carbonate coating
VIL-2	0.0209	VIL05-1B-1T-119, 42-49	45.4	gastropods
		VIL05-1B-1T-121, 33-35	45.7	gastropods
VIL-3	0.0261	VIL05-1B-1T-142, 0-10	52.2	gastropods
	0.0216	VIL05-1B-1T-143, 7-11	52.7	gastropods
	0.0429	VIL05-1B-1T-143, 27-30	52.9	gastropods
VIL-4	0.0852	VIL05-1B-1T-144, 0-5	53.1	gastropods
	0.0261	VIL05-1B-1T-144, 20-22	53.2	gastropods
	0.0216	VIL05-1B-1T-144, 25-33	53.3	gastropods
VIL-5	0.0429	VIL05-1B-1T-118, 40	45.1	Carbonate coating
VIL-6	0.0852	VIL05-1B-1T-112, 10-12	43.4	Carbonate coating

B)

Sample ID	^{238}U Ppb		^{232}Th ppt		$\delta^{234}U$ measured[a]		$[^{230}Th/^{238}U]$ activity[c]		$[^{230}Th/^{232}Th]$ ppm[d]		Age uncorrected		Age corrected [c,e]		$\delta^{234}U_{initial}$ corrected[b]	
VIL-1	564	± 1.5	456003	± 7657	957.8	± 4.6	3.91658	± 0.092	79.8	± 2.3	-	-	-	-	-	-
VIL-2	167	± 0.6	90183	± 567	78.8	± 6.4	1.04223	± 0.028	31.8	± 0.9	313 784.7	± 51327.8	299 669.8	± 45407.0	183.8	± 33.3
VIL-3	100	± 0.4	2738	± 29	148.0	± 8.0	1.02330	± 0.014	614.3	± 10.5	216 876.0	± 10444.8	216 246.9	± 10389.0	272.7	± 16.9
VIL-4	111	± 0.5	2276	± 34	104.0	± 8.8	1.04494	± 0.013	840.5	± 16.2	276 135.6	± 19331.9	275 648.7	± 19246.1	226.6	± 23.4
VIL-5	337	± 0.7	464119	± 8122	18.0	± 2.6	1.48947	± 0.102	17.8	± 1.3	-	-	-	-	-	-
VIL-6	190	± 0.4	41233	± 188	2.4	± 2.4	1.16244	± 0.011	88.1	± 0.9	-	-	-	-	-	-

Analytical errors are 2σ of the mean. [a] $\delta^{234}U = ([^{234}U/^{238}U]_{activity} - 1) \times 1000$; [b] $\delta^{234}U_{initial}$ corrected was calculated based on ^{230}Th age (T), i.e., $\delta^{234}U_{initial} = \delta^{234}U_{measured} X e^{\lambda 234 * T}$, and T is corrected age. [c] $[^{230}Th/^{238}U]_{activity} = 1 - e^{-\lambda 230 T} + (\delta^{234}U_{measured}/1000)[\lambda_{230}/(\lambda_{230} - \lambda_{234})](1 - e^{-(\lambda 230 - \lambda 234) T})$, where T is the age. Decay constants are 9.1577 x 10^{-6} yr^{-1} for ^{230}Th, 2.8263 x 10^{-6} yr^{-1} for ^{234}U, and 1.55125 x 10^{-10} yr^{-1} for ^{238}U (Cheng et al., 2000). [d] The degree of detrital ^{230}Th contamination is indicated by the $[^{230}Th/^{232}Th]$ atomic ratio instead of the activity ratio. [e] Age corrections were calculated using an average crustal $^{230}Th/^{232}Th$ atomic ratio of 4.4 x 10^{-6} ± 2.2 x 10^{-6}. Those are the values for a material at secular equilibrium, with the crustal $^{232}Th/^{238}U$ value of 3.8. The errors are arbitrarily assumed to be 50%.

Table 4. Dose rate data, multi-grain aliquot additive dose equivalent doses (D_e) and polymineral fine-grain IRSL ages for the VIL samples.

Sample	Sample depth (m)	Grain size (μm)	water content [a]	*a*-value [b]	Total dose rate [c, d]	D_e (Gy) [d]	OSL age (ka) [d]
MAD-5172SDA	18.0	2-10	26	0.08	0.83 ± 0.06	34 ± 1	40.4 ± 3.5
MAD-5173SDA	47.0	2-10	26	0.11	1.05 ± 0.07	76 ± 2	72.5 ± 5.1
MAD-5196SDA	54.0	2-10	20	0.16	1.27 ± 0.08	119 ± 4	93.6 ± 6.8
MAD-5200SDA	71.0	2-10	30	0.22	2.84 ± 0.22	329 ± 3	115.9 ± 9.0
MAD-5203SDA	73.0	2-10	30	0.08	0.94 ± 0.04	114 ± 6	120.8 ± 8.2

[a] Field water content, expressed as % of dry mass of mineral fraction, with an assigned relative uncertainty of ±1%.
[b] Alpha effectiveness value used for alpha dose rate calculation, determined using the approach of Zimmerman (1972).
[c] Total dose rate comprises alpha, beta, gamma and cosmic-ray contributions. Beta and gamma dose rates were determined from ^{40}K, ^{238}U and ^{232}Th activities calculated on dried and homogenised, bulk sediment samples using a combination of beta counting and thick source alpha counting. The conversion factors of Nambi and Aitken (1986) were used to derive dose rate estimates from measured activities.
[d] Mean ± total uncertainty (68% confidence interval), calculated as the quadratic sum of the random and systematic uncertainties.

Table 5. Dose rate data, single-grain equivalent doses (D_e) and quartz OSL ages for the VIL samples

Sample	Sample depth (m)	Grain size (μm)	Measured water content [a]	Compaction-corrected water content [b]	Environmental dose rate (Gy/ka)				Equivalent dose (D_e) data				OSL age (ka) [e, f]
					Beta dose rate [c]	Gamma dose rate [c]	Cosmic dose rate [d]	Total dose rate [e, f]	No. of grains [g]	Overdis-persion (%) [h]	Age model [i]	D_e (Gy) [e]	
V49	27.0	180 - 250	27 ± 7	30 ± 8	1.60 ± 0.08	0.95 ± 0.03	0.05 ± 0.01	2.64 ± 0.21	72 / 1100	29 ± 4	MAM-4	129 ± 18	49.0 ± 7.9
V58	31.6	212 - 250	13 ± 3	15 ± 4	0.91 ± 0.05	0.63 ± 0.03	0.04 ± 0.01	1.62 ± 0.10	93 / 1000	37 ± 4	MAM-4	116 ± 13	71.6 ± 9.4
V67	36.6	212 - 250	19 ± 5	21 ± 5	1.53 ± 0.08	1.01 ± 0.03	0.04 ± 0.01	2.61 ± 0.17	60 / 1000	18 ± 6	CAM	191 ± 9	73.2 ± 6.1
V99	51.8	212 - 250	12 ± 3	14 ± 4	0.85 ± 0.04	0.60 ± 0.02	0.02 ± 0.01	1.51 ± 0.08	75 / 1000	29 ± 4	MAM-4	128 ± 16	84.6 ± 11.3
V110	56.8	180 - 250	27 ± 7	35 ± 9	0.91 ± 0.05	0.64 ± 0.03	0.02 ± 0.01	1.60 ± 0.14	71 / 900	29 ± 4	MAM-4	167 ± 16	104.5 ± 14.1
V117	59.8	212 - 250	24 ± 6	28 ± 7	0.81 ± 0.05	0.57 ± 0.02	0.02 ± 0.01	1.43 ± 0.11	94 / 1200	26 ± 3	MAM-4	180 ± 18	126.3 ± 16.2
V127	63.9	212 - 250	13 ± 3	16 ± 4	1.23 ± 0.06	0.77 ± 0.03	0.02 ± 0.01	2.06 ± 0.12	81 / 1300	13 ± 3	CAM	264 ± 9	128.1 ± 9.1
V135	67.5	212 - 250	23 ± 6	28 ± 7	0.95 ± 0.05	0.64 ± 0.03	0.02 ± 0.01	1.64 ± 0.14	63 / 1000	22 ± 4	CAM	220 ± 10	134.1 ± 12.8
V148	72.7	212 - 250	14 ± 3	19 ± 5	1.02 ± 0.05	0.66 ± 0.02	0.02 ± 0.01	1.72 ± 0.11	75 / 1000	22 ± 4	CAM	236 ± 11	137.0 ± 10.9

[a] Field water content, expressed as % of dry mass of mineral fraction, with an assigned relative uncertainty of ±25%.

[b] Corrected field water contents used to calculate the final OSL ages for these samples. Full details of the procedures used to derive these compaction-correction water contents are provided in the Supplementary Information. This correction has been included because of the relatively thick sediment overburdens affecting these samples and, hence, the increased likelihood of sediment compaction and dewatering effects with time.

[a] Measurements made on dried and powdered samples by high-resolution gamma-ray spectrometry. Specific activities have been converted to dose rates using the conversion factors given in Guérin *et al.* (2011), making allowance for beta-dose attenuation (Mejdahl, 1979; Brennan, 2003).

[d] Cosmic-ray dose rates were calculated using the approach of Prescott and Hutton (1994) and assigned a relative uncertainty of ±10%.

[e] Mean ± total uncertainty (68% confidence interval), calculated as the quadratic sum of the random and systematic uncertainties.

[f] Includes an internal dose rate of 0.03 Gy/ka with an assigned relative uncertainty of ±30%.

[g] Number of D_e measurements that passed the SAR rejection criteria and were used for D_e determination / total number of grains analysed.

[h] The relative spread in the D_e dataset beyond that associated with the measurement uncertainties for individual D_e values, calculated using the central age model (CAM) of Galbraith *et al.* (1999).

[i] Age model used to calculate the sample-averaged D_e value for each sample. MAM-4 = 4-parameter minimum age model of Galbraith *et al.* (1999). The MAM-4 has been preferred over the 3-parameter minimum age model (MAM-3) for these single-grain datasets on statistical grounds using the maximum log likelihood (L_{max}) score criterion outlined by Arnold et al. (2009). MAM-4 D_e estimates were calculated after adding, in quadrature, a relative error of 10% to each individual D_e measurement error to approximate the minimum underlying dose overdispersion observed in the single-grain dose-recovery test and in an 'ideal' (well-bleached and unmixed) sedimentary sample from this core (sample V127).

[j] Total uncertainty includes a systematic component of ±2% associated with laboratory beta-source calibration.

Table 6. High-resolution gamma spectrometry results and daughter-to-parent isotopic ratios for the VIL single-grain OSL samples.

Sample	Sample depth (m)	Radionuclide specific activities (Bq/kg) [a, b]						Daughter/ parent isotopic ratio		
		^{238}U	^{226}Ra	^{210}Pb	^{228}Ra	^{228}Th	^{40}K	$^{226}Ra/^{238}U$	$^{210}Pb/^{226}Ra$	$^{228Th}/^{228}Ra$
V49	27.0	22.5 ± 4.4	25.5 ± 1.9	26.1 ± 2.2	38.5 ± 3.3	39.0 ± 2.8	763 ± 26	1.13 ± 0.24	1.02 ± 0.12	1.01 ± 0.11
V58	31.6	28.9 ± 4.8	25.0 ± 1.7	25.2 ± 3.2	23.8 ± 2.9	24.2 ± 1.4	303 ± 11	0.86 ± 0.16	1.01 ± 0.15	1.02 ± 0.14
V67	36.6	27.5 ± 4.8	22.8 ± 2.3	25.0 ± 3.2	46.8 ± 5.6	46.6 ± 5.3	624 ± 21	0.83 ± 0.17	1.09 ± 0.18	1.00 ± 0.16
V99	51.8	16.4 ± 2.7	18.0 ± 1.3	18.2 ± 2.1	25.5 ± 3.1	26.1 ± 3.4	302 ± 11	1.10 ± 0.19	1.01 ± 0.14	1.02 ± 0.18
V110	56.8	31.4 ± 4.3	32.6 ± 2.3	34.8 ± 4.2	26.5 ± 3.2	26.8 ± 2.9	367 ± 13	1.04 ± 0.16	1.07 ± 0.15	1.01 ± 0.16
V117	59.8	23.1 ± 4.8	23.7 ± 2.5	23.8 ± 2.8	25.4 ± 3.1	25.0 ± 5.4	317 ± 11	1.03 ± 0.24	1.00 ± 0.16	0.99 ± 0.24
V127	63.9	24.4 ± 4.1	22.9 ± 1.7	22.0 ± 2.8	29.2 ± 3.5	30.2 ± 2.1	477 ± 16	0.95 ± 0.17	0.96 ± 0.14	1.03 ± 0.14
V135	67.5	29.1 ± 4.9	28.9 ± 2.1	27.5 ± 3.4	29.0 ± 3.5	23.6 ± 4.1	380 ± 13	0.99 ± 0.18	0.95 ± 0.14	0.81 ± 0.17
V148	72.7	20.2 ± 2.7	21.3 ± 1.5	22.0 ± 2.7	25.3 ± 3.0	24.9 ± 2.1	397 ± 13	1.06 ± 0.16	1.03 ± 0.14	0.98 ± 0.14

[a] Measurements made on dried and powdered samples by high-resolution gamma-ray spectrometry.
[b] Mean ± total uncertainty (68% confidence interval), calculated as the quadratic sum of the random and systematic uncertainties.

Figure 1. A. Location of Cañizar de Villarquemado Basin. B. Map of the watershed and maximum surface area of the wetland prior to drainage.

A

B

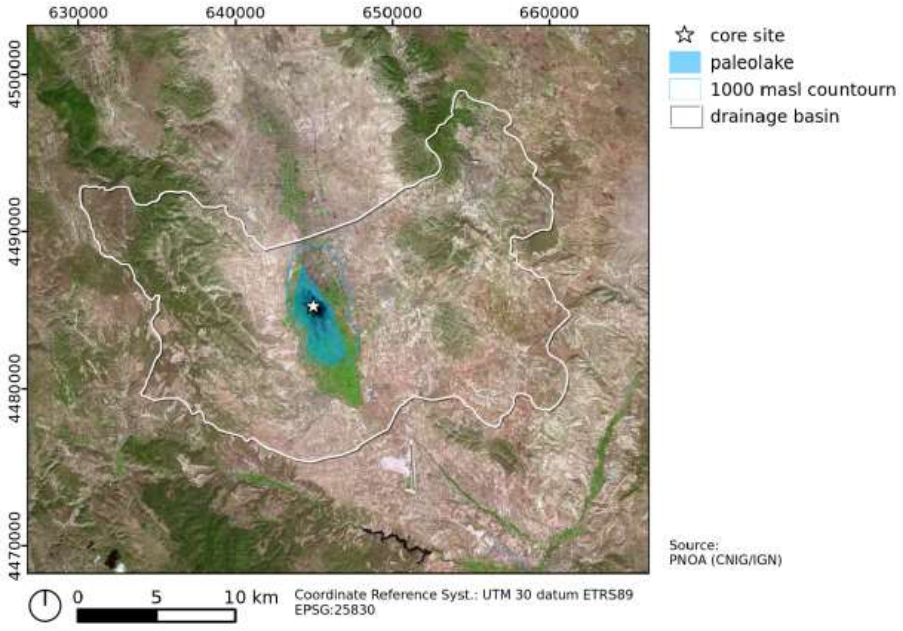

Figure 2. Stratigraphy of the VIL sequence: sedimentary facies and associations, unit depositional environments and location of samples for different dating methods.

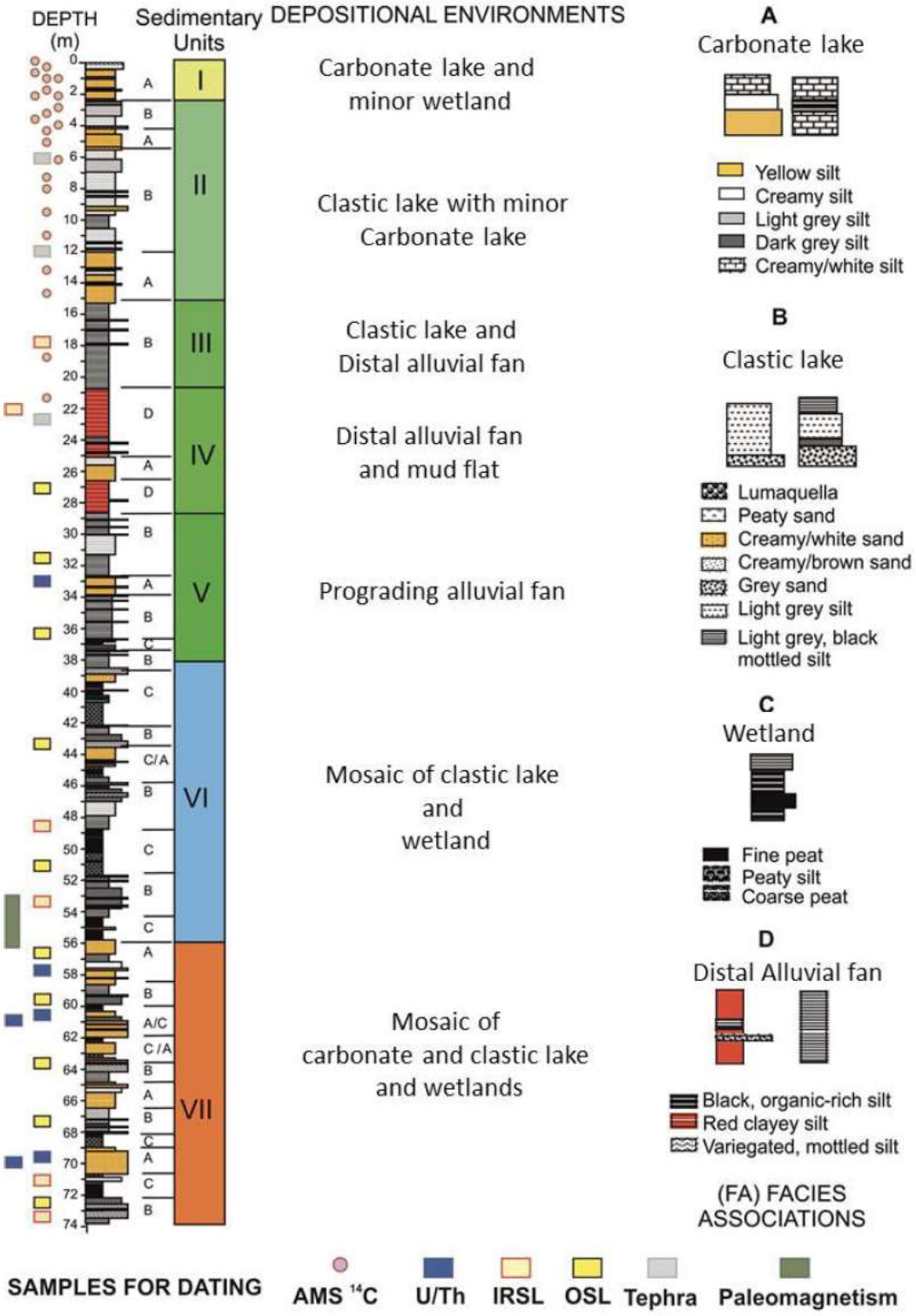

Figure 5. The Bayesian Age model for VIL sequence with all the dates included (A) and the final result with the 30 selected dates and the main sedimentation rate changes indicated (B).

A)

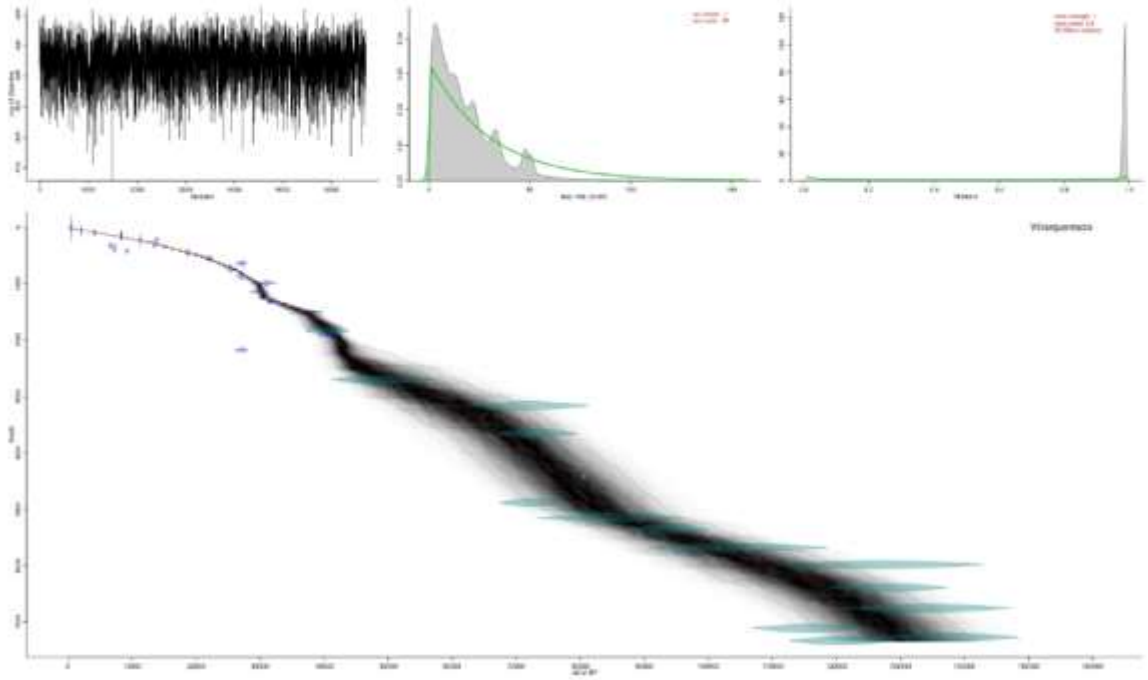

B)

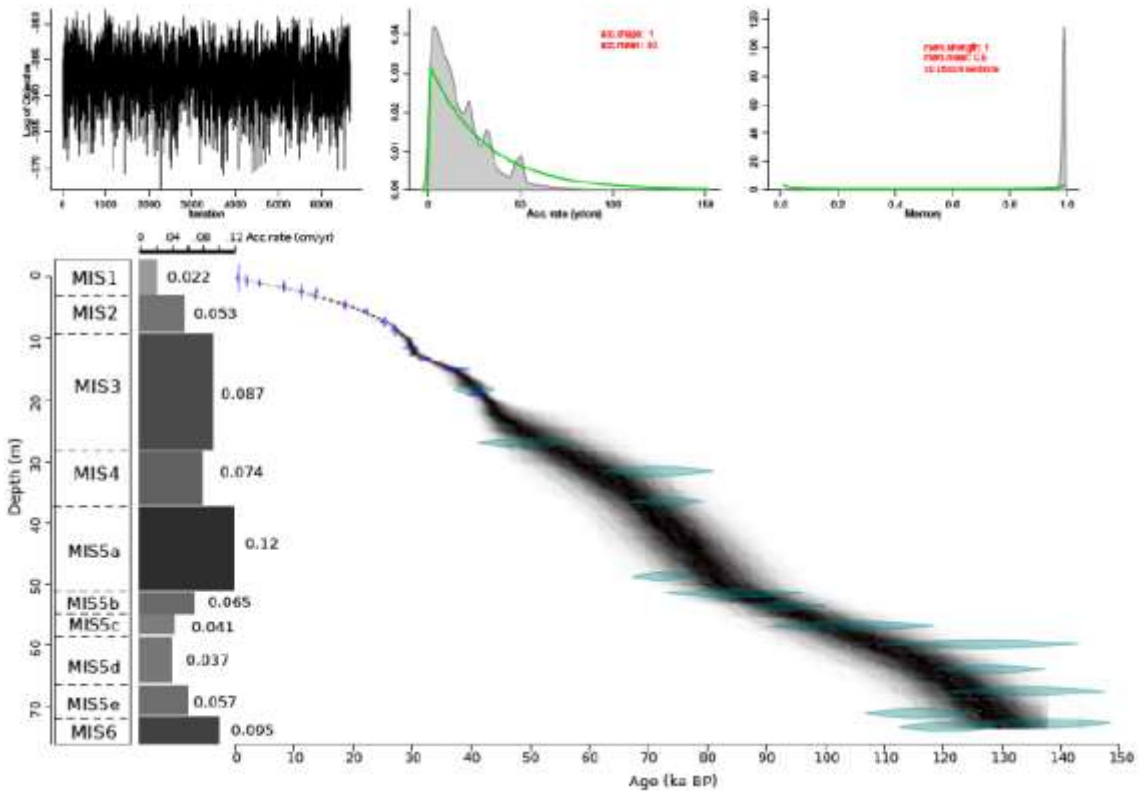

Figure 6. Main geochemical and palynological data of VIL sequence plotted in age with both sedimentological units (on the left) and MIS periods (on the right) indicated. Chronological limits for MIS periods follow Lisiecki and Raymo (2005) and Rasmussen et al. (2014) while stadials and interstadials into MIS 5 chronology follow Martrat et al. (2004). Pollen groups are composed by the following taxa: Mediterranean includes evergreen *Quercus*, *Viburnum*, *Buxus*, Oleaceae, *Pistacia*, *Rhamnus*, *Myrtus*, Thymelaeaceae, *Arbutus unedo*, Cistaceae and *Helianthemum*. Steppe includes *Ephedra distachya* and *E. fragilis* types and Chenopodiaceae. Local moisture is formed by aquatics and Pterydophyta: Cyperaceae, Typhaceae, *Juncus*, *Sparganium*, *Thalictrum*, *Lythrum*, *Stratiotes*, *Utricularia*, *Ledum palustre*, *Ranunculus*, *Pedicularis*, *Myriophyllum*, *Lemna*, *Nymphaea*, *Nuphar*, *Potamogeton*, *Isoetes*, *Alisma*, *Callitriche*, *Asplenium*, Monolete, Trilete, *Polypodium*, *Botrychium*, *Pteris*, *Equisetum* and *Selaginella*. Shaded grey bands show intervals with low pollen productivity in MIS 5b, MIS 3 and MIS 2.

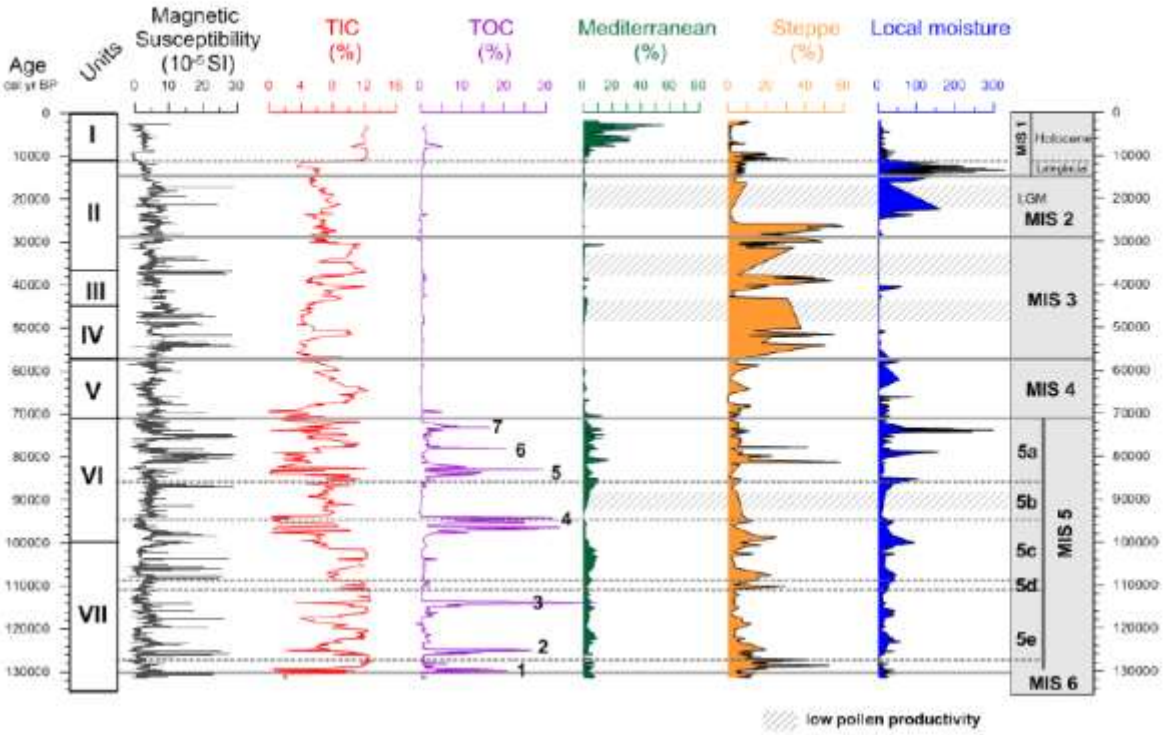

(a) V127: 300 Gy dose-recovery test

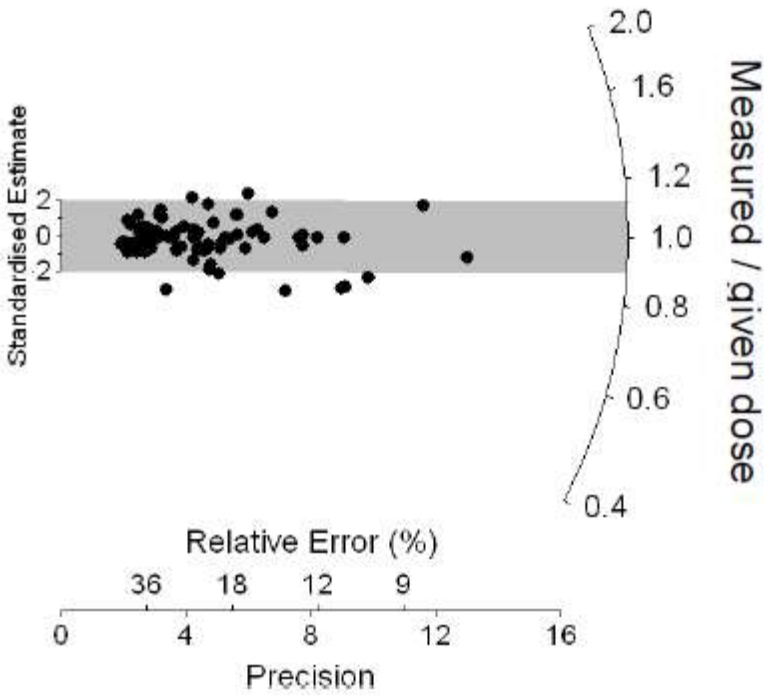

(b) V127: Natural D_e values

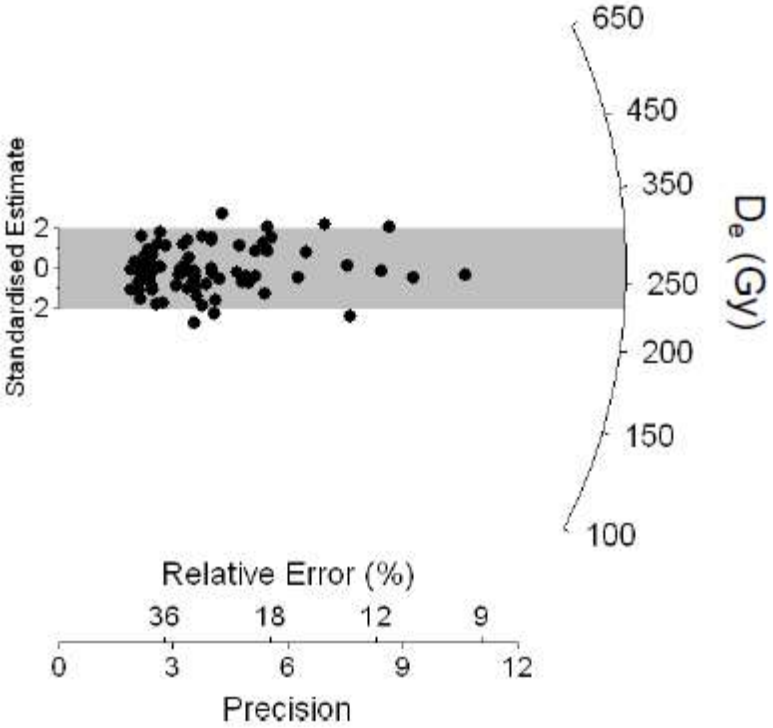

(c) V99: Natural D_e values

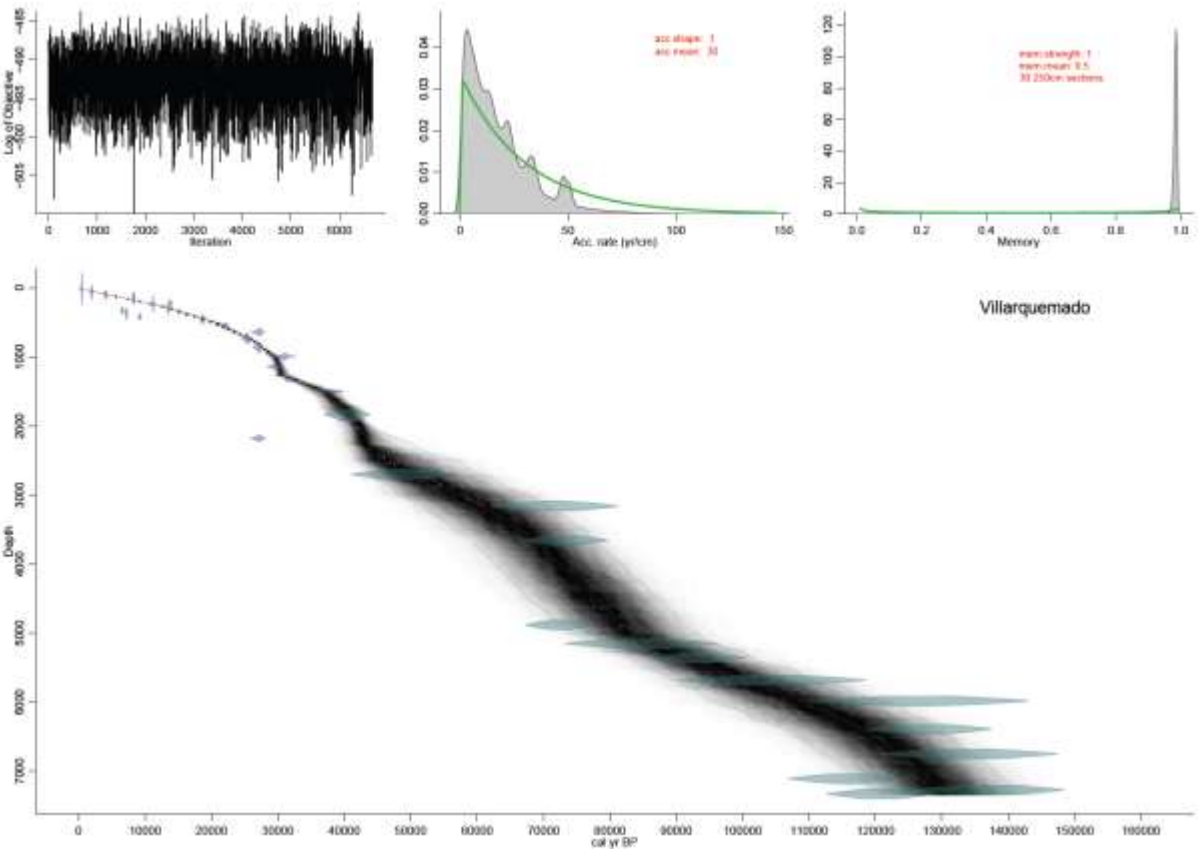
Villarquemado
Log of Objective
Iteration
Acc. rate (yr/cm)
Memory
Depth
cal yr BP

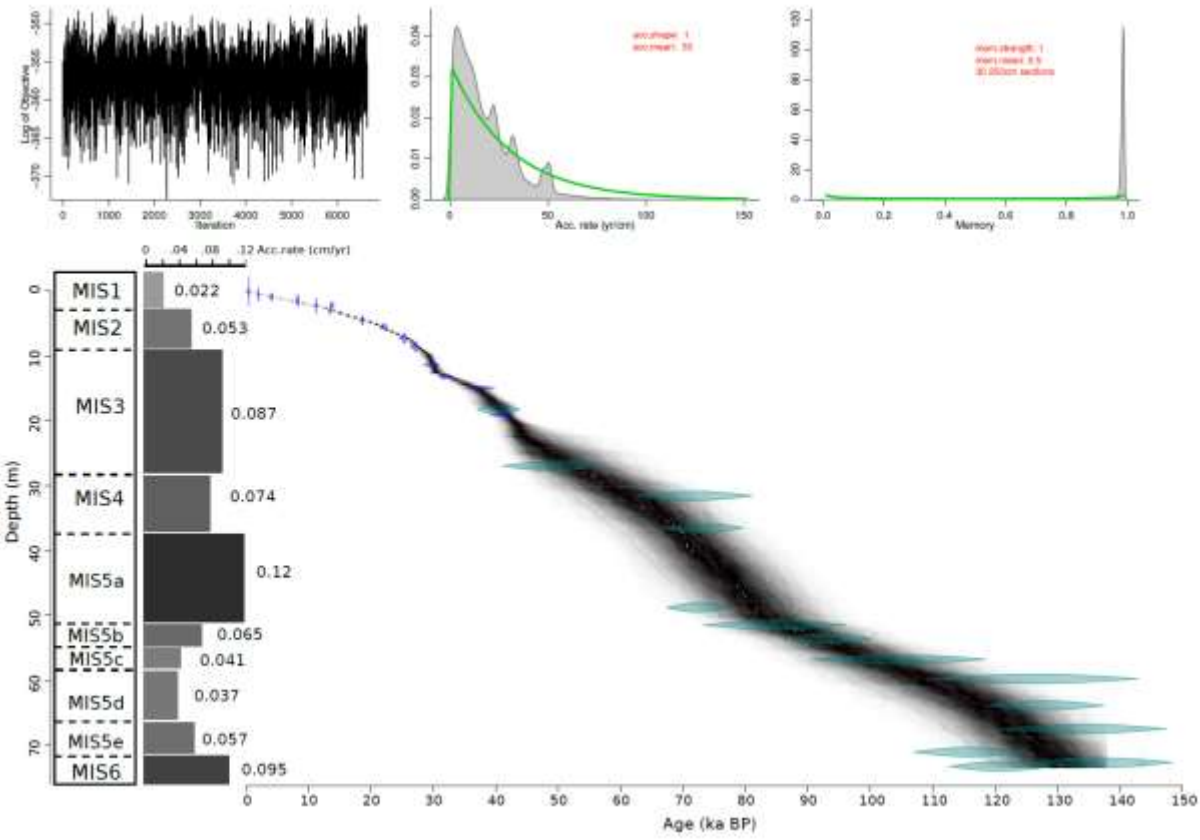
Log of Objective
Iteration
Acc. rate (yr/cm)
Memory
0 .04 .08 .12 Acc.rate (cm/yr)
MIS1
MIS2
MIS3
MIS4
MIS5a
MIS5b
MIS5c
MIS5d
MIS5e
MIS6
0.022
0.053
0.087
0.074
0.12
0.065
0.041
0.037
0.057
0.095
Depth (m)
Age (ka BP)

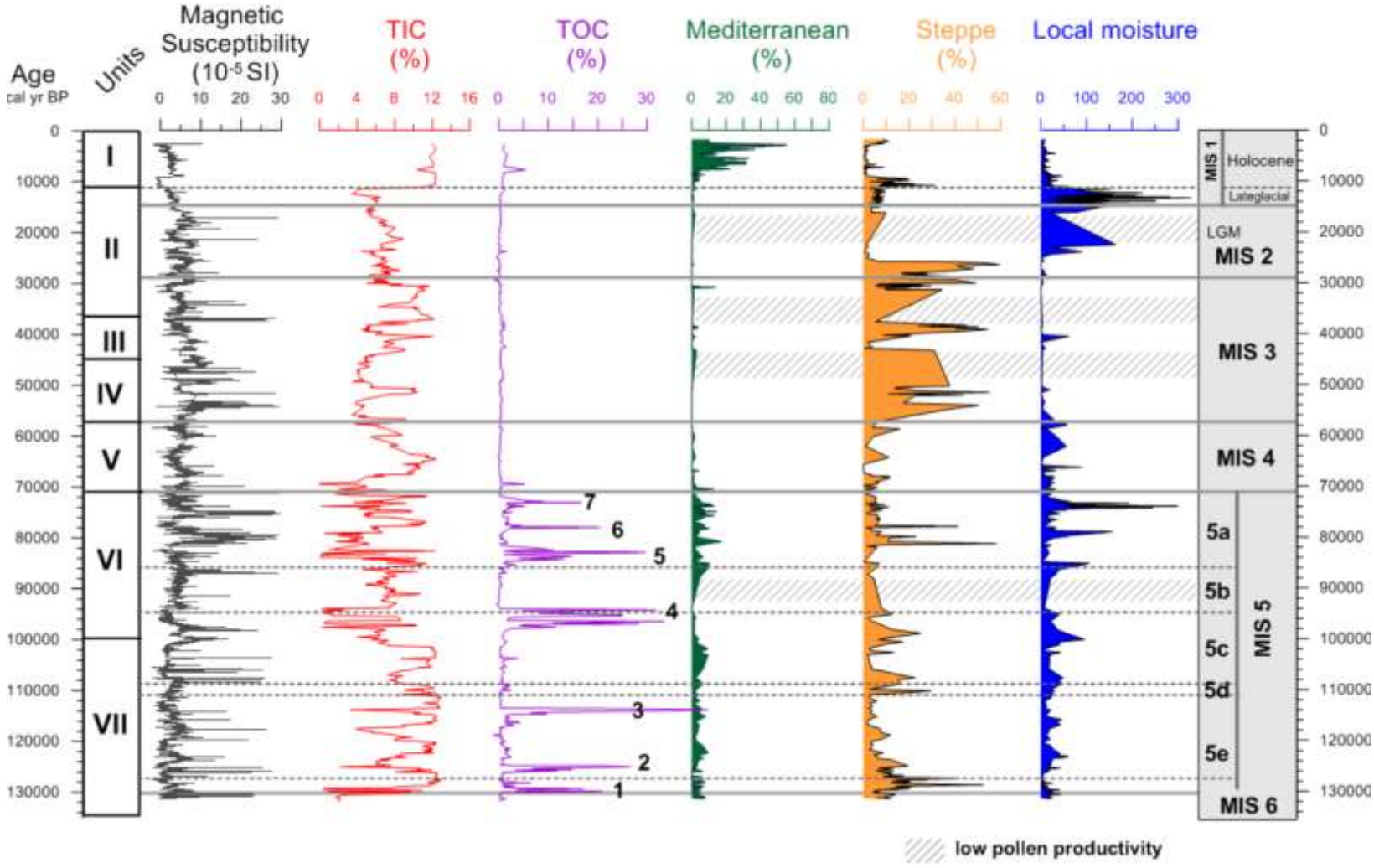
Age
cal yr BP
Units
Magnetic Susceptibility (10^{-5} SI)
TIC (%)
TOC (%)
Mediterranean (%)
Steppe (%)
Local moisture
0 10 20 30
0 4 8 12 16
0 10 20 30
0 20 40 60 80
0 20 40 60
0 100 200 300
0
10000
20000
30000
40000
50000
60000
70000
80000
90000
100000
110000
120000
130000
I
II
III
IV
V
VI
VII
7
6
5
4
3
2
1
MIS 1
Holocene
Lateglacial
LGM
MIS 2
MIS 3
MIS 4
5a
5b
5c
5d
5e
MIS 5
MIS 6
low pollen productivity